

Experimental Investigation of the Stability of Keplerian Disks

by

Ruvim Kondratyev

Submitted in Partial Fulfillment of the
Requirements for the Degree

Bachelor of Arts

Supervised by
Dr. Daniel Borrero-Echeverry

Department of Physics

Willamette University, College of Liberal Arts
Salem, Oregon

2017

Presentations and publications

- R. Kondratyev and D. Borrero-Echeverry. “Experimental Investigation of the Stability of Keplerian Disks in 2D.” Physics Symposium of Willamette University and Linfield College, Poster. Willamette University, 2017.
- R. Kondratyev. “Experimental Investigation of the Stability of Keplerian Disks.” Student Scholarship Recognition Day (SSRD). Willamette University, 2017.
- R. Kondratyev and H. Cheng, “Numerical Analysis of the Hybrid Particle Filter on a Chaotic System,” 23rd Annual Murdock College Science Research Conference, Vancouver, WA, 2014.
- R. Kondratyev and H. Cheng, “Numerical Analysis of the Hybrid Particle Filter on a Chaotic System,” CCSC-NW conference, Gonzaga University, 2014.
- R. Kondratyev, D. Livingston, and H. Cheng, “Numerical Experiments on Improving Particle Filter Performance,” SCRP Symposium, Willamette University, 2014.

Acknowledgments

This project could not have been done without a lot of support. Professor Watkins was an invaluable resource for my questions about astrophysics. Chemical hygiene officer and chemistry stockroom manager Leslie Coop provided me with many of the chemistry tools, such as pasteur pipets, a wash bottle, a chemical storage container, a waste container, and some safety advice. Thanks a lot to Professor Altman for allowing me to use his lab's super-accurate balance to measure the copper sulfate mass before I dissolved it into solution. Thanks to Professor Kleinert for her lab's gaussmeter and for her help and concern throughout the year. As my academic advisor, she also helped me not overload myself, so I could focus on this thesis. I am also thankful to my research advisor Professor Borrero for putting up with me and for buying all the lab equipment, including the fancy glassware. Even after the semester was over, and even though he was probably tired, he still read and re-read my thesis, sharing the comments on Google Drive. And Willamette University overall was very friendly to my project, including the free drinking straws and spoons from the Bistro that I used for the copper sulfate and for seeding the experimental apparatus with imaging beads. I am thankful to my family, who have done my house work and chores for me, so that I could devote my attention to school-work and to this thesis. They were very supportive of me.

Technical Abstract

Matter in astrophysical disks is believed to flow about the disk's center with a Keplerian angular velocity, $\Omega_k \propto r^{-3/2}$, where r is the radial distance. The matter accretes (accumulates) at the disk center by shedding its angular momentum and hence allowing itself to lose potential energy. The angular momentum transport would be a diffusion process under local viscosity alone, which would make the accretion process very slow. The rate of angular momentum transport can be enhanced if the flow is turbulent, but turbulence requires an instability to cause it. Keplerian flow is believed to be stable, but there is no definite proof yet. Astrophysical accretion disks need an instability mechanism to enhance angular momentum transport, and one possibility is a purely hydrodynamic instability due to the Keplerian profile itself. This project built a table-top experimental setup where electric current was driven through a water cell, forcing the water, and we studied the resulting flow profile. Particle image velocimetry (PIV) was used to find the angular velocity profiles. The A_p constant was found to be $A_p = (627 \pm 2) \frac{\text{mm}^3 \text{ rad}}{\text{A G s}}$. We found a flow profile of $\Omega(r) \propto r^P$ where $P = -3.52 \pm 0.08$ for a magnetic field profile of $B(r) \propto r^{-1.5}$, and $P = -1.157 \pm 0.009$ for $B(r) \propto r^{0.6}$. The former was in agreement with the expected angular velocity, while the latter was not quite the predicted $P = -1.5$ for a Keplerian flow. From the observations so far, no instability was observed, suggesting that either Keplerian flow really is stable, or more research needs to be done.

General Abstract

Astrophysical accretion disks form as matter spirals inward into a heavy central object like a black hole. They are so large that viscosity, the property of how thick the gas in the disk is, cannot make the disk form and accrete fast enough. Just by viscosity alone, the disk will take 3×10^{14} years to form, which is much longer than the age of the universe! There is a lot of debate in the astrophysics literature about why accretion disks form so quickly, but the gist of it is that there must be a mechanism making the gas flow in the disk unstable. Instabilities lead to turbulence, which mixes momentum of the gas particles very quickly, and that is good for making the disk form and accrete quickly. There are many candidate sources of this turbulence, but this thesis explored the stability of the Keplerian velocity profile itself, which these accretion disks possess. Two table-top setups were built in which we used electromagnetic forces to drive flow in a thin liquid layer. One had an arbitrary magnetic field profile - we chose Keplerian - to test our model equations, and the other had a field that would create a Keplerian fluid flow. We had a video camera monitor the movement of particles floating at the surface of a thin liquid layer, and we used a computer to analyze the flow profile. The flow behaved mostly like our equation predicted, but the latter setup's fluid profile was not quite Keplerian. The flow closely approximated the Keplerian profile, and, while more data should be taken, results so far suggest that Keplerian flow is stable.

Table of Contents

Acknowledgments	iii
Technical Abstract	iv
General Abstract	v
List of Tables	viii
List of Figures	ix
1 Introduction	1
1.1 Accretion Disks	1
1.2 Experimental Setup	6
1.3 Research Context	7
2 Background	10
2.1 Astrophysical Accretion Disks	10
2.2 Keplerian Velocity Profile	11
2.3 Lorentz Force	12
3 Methods	14
3.1 Design of Setup-3	14
3.2 Magnetic Field	17
3.3 Conducting the Experiment	20
3.4 Setup-1 as a Test	22
3.5 Taking and Processing Image Data	29
3.6 Angular Velocity's Proportionality Constant to the Magnetic Field	34

4	Results and Discussion	36
4.1	High-level trends from Setup-3	36
4.2	A snapshot of Setup-3	40
4.3	A snapshot of Setup-1	41
4.4	Final Thoughts	42
	Bibliography	44
A	Safety Tips	47
A.1	3D Printer Safety	47
A.2	Metal-Cutting Safety	48
A.3	Chemical Safety	48
B	Finding Dipole Magnetization Constant	50
B.1	Magnetization Constant from K&J Magnetics Calculator	50
B.2	Measuring the Constant from an Actual Magnet	53
B.3	Using the Dipole Magnetization Constant	56
C	Magnet Slot Radius	57
D	Optimizing Magnet Arrangement	61
D.1	Installing Bokeh	61
D.2	Using Python Code	62
E	Parameters for Setup-1, Setup-2, and Setup-3	68
F	Our 3D Parts in FreeCAD	71
G	Taking Data	78
H	Linear Regression	81

List of Tables

C.1	The magnet slot test tray, where each slot was given one radius in the CAD model, but ended up with a slightly different radius due to 3D printing imperfections.	58
E.1	Magnet arrangement parameters' optimization results for Setup-1. The variables are i , the ring number, N_i , the number of magnets in the i th ring, R_i , the radius of the ring, H_i , the height of that ring, and A_i , the angle by which the ring should be rotated about the Z-axis.	69
E.2	Magnet arrangement parameters for Setup-2. The variables are i , the ring number, N_i , the number of magnets in the i th ring, R_i , the radius of the ring, H_i , the height of that ring, and A_i , the angle by which the ring should be rotated about the Z-axis.	69
E.3	Magnet arrangement parameters for Setup-3. The variables are i , the ring number, N_i , the number of magnets in the i th ring, R_i , the radius of the ring, H_i , the height of that ring, and A_i , the angle by which the ring should be rotated about the Z-axis.	70

List of Figures

1.1	An artist’s impression of a black hole pulling matter from a star. The matter first has to orbit the black hole before it falls in. Public domain by NASA [NASa].	2
1.2	In an orbit, angular momentum is conserved. When radial position, r , is small, the velocity, v , has to be large to keep angular momentum constant.	3
1.3	Before coming to the center, water in a funnel first rotates due to inertia and conservation of angular momentum; matter in an accretion disk undergoes the same process.	4
1.4	In kinetic theory, molecules fly around and run into each other, exchanging kinetic energy.	5
1.5	A water cell that has cylindrical symmetry can be used to drive a circular water flow. There are copper electrodes (the “circular pieces of metal”) touching the water: one in the center, and one on the outer wall.	6
1.6	An array of magnets arranged in a special way can create our desired magnetic field profile.	7
2.1	An accretion disk can be modeled as a thin disk whose matter orbits at an angular velocity $\Omega(r)$ [Shu92].	10
3.1	An assembly drawing of Setup-3. At the bottom is a stand that holds up a tray with a magnet arrangement. This magnet arrangement creates a magnetic field at the surface of the water in the cell sitting on top of the magnet tray. A cylindrical part centers the system.	15
3.2	The alligator clip wire goes under the setup, through the cylinder, and onto the electrode.	16

3.3	Setup-3 magnet tray cross section. The magnets are inserted by pushing down on them from the top, and they do not stick out on the top when pushed all the way in. To take them out, the “rescue holes” can be used to push them out with a thin rod. The rescue holes go all the way to the bottom of the magnet tray.	17
3.4	We measured the magnetic field at different distances from the center for Setup-3 using a gaussmeter and a few tools that we custom 3D-printed for positioning the magnetic field probe accurately. . .	18
3.5	The black curve is the theoretically predicted magnetic field profile for the Setup-3 magnet arrangement. Orange is a fit to show that it is roughly square-root shaped, and green dots are measurements using a gaussmeter.	19
3.6	The radial, azimuthal, and vertical components of the predicted magnetic field, in gauss, in cylindrical coordinates for Setup-3. . .	20
3.7	The Setup-3 system: a magnet tray, with a cylindrical water tray sitting on top of it.	21
3.8	Experimental setup. There is an IDS uEye camera fixed above the system, a grid of LED lights fixed next to it, a current driver hooked up to the system, and an ammeter to monitor the current accurately.	22
3.9	An assembly drawing of Setup-1. The magnet tray is a complex part with removeable rings of magnets. The water cell sits at the top as usual.	23
3.10	A test magnet ring with cylindrical slots for five magnets. The ring also has flat slots for copper shim stock to go through and hold the magnets in place. In case the magnets get stuck, there are small holes on the opposite side for pushing the magnets out with a thin tool. The magnets were inserted with the north (N) pole directed vertically <i>up</i>	24
3.11	Top-down view photos of the system. The magnets are inside the rings where the copper shim stock pieces are; the shim stock pieces are for holding the rings in place, as well as for preventing any magnets from jumping out.	24
3.12	Perspective-view photos of the system.	25
3.13	The radial, azimuthal, and vertical components of the predicted magnetic field, in gauss, in cylindrical coordinates for Setup-1. . .	26

3.14	We measured the magnetic field at different distances from the center for Setup-1 using a caliper and a gauss meter. The gauss meter was carefully taped to a plastic piece of width 4.5 mm, almost the 5 mm for the water level, and placed on top of the water cell's floor for measuring.	27
3.15	The vertical component, B_z , magnetic field profile as a function of radial position for Setup-1. The green dots are the measurement samples from the actual measurements done on the system we built, as measured by the method in Fig. 3.14. The orange line is a $r^{-3/2}$ curve scaled to fit the green dots.	28
3.16	The bottom part: the magnet tray; some of the outer-most posts broke a little during printing, but it mostly turned out fine. . . .	28
3.17	The frames after subtracting the background and filling unimportant pixels with zeros.	29
3.18	Velocity field of validated vectors.	30
3.19	Radial velocity, $(\frac{d\vec{r}}{dt})_r$, for each setup.	32
3.20	Angular velocity, $(\frac{d\vec{r}}{dt})_\theta$, for each setup.	32
3.21	Measured angular velocity in log-space plotted with a linear regression fit.	33
3.22	Measured angular velocity plotted with a power fit and an expected angular velocity based on Eq. 2.9 and the constant A_p found in Section 3.6.	33
4.1	The angular velocity is proportional to the current.	37
4.2	The angular velocity's power profile jumps around a lot for small electric currents but evens out to around -1.2 at larger currents.	38
4.3	The constant, A_p , is chaotic for very small currents, but evens out starting from around 20 mA.	39
4.4	Setup-3. After the PIV analysis, vector fields were obtained representing particle velocities, (u, v) . The velocities' magnitudes, v_θ , are shown in false-color on the left, and the actual (u, v) vector field is shown on the right. The vectors are pointing mostly in the counter-clockwise direction.	40
4.5	Setup-3. Left: The flattened $(r, \Omega(r))$ data (flattened means we turned the 2D data into a 1D array) was fit against a power law, $y = Ar^P$. The fit was only done on the part of the curve that fit a power law. Right: The A_p samples (see previous chapter) and their mean value as the green curve.	41

4.6	Setup-1. After the PIV analysis, vector fields were obtained representing particle velocities, (u, v) . The velocities' magnitudes, v_θ , are shown in false-color on the left, and the actual (u, v) vector field is shown on the right. The vectors are pointing mostly in the counter-clockwise direction.	42
4.7	Setup-1. Left: The flattened $(r, \Omega(r))$ data was fit against a power law, $y = Ar^P$. The fit was only done on the part of the curve that fit a power law. Right: The A_p samples (see previous chapter) and their mean value as the green curve.	42
B.1	Magnetic field strength calculated for our N42 1/4" \times 1/4" magnet from the K&J Magnetics website [K&]. A magnetic dipole fit has been placed over the tail, where position is at least 0.4 in from the center of the magnet. The position was measured vertically from the center of a magnet that is oriented with its north axis up. . .	51
B.2	The intermediate $(r, r^3B(r)/2)$ form used to fit M , the dipole magnetization constant.	52
B.3	The K&J Magnetics finite element magnetic field calculator was used to find the predicted magnetic fields directly above the magnet, a distance r away from its center. Image by [K&].	53
B.4	We designed and printed six rulers for accurately placing our gaussmeter probe at known positions above a magnet. The slots are spaced such that the slots' centers are 3 mm apart.	54
B.5	The slots were just a little bit too big, so we put tape around the probe and magnet in order for them to fit perfectly.	54
B.6	Magnetic field strength measured for our N42 1/4" \times 1/4" magnet using the Kleinert lab's gaussmeter. The position was measured vertically from the center of the magnet.	55
B.7	The intermediate M form (Eq. B.3) used to fit the curve in Fig. B.6.	56
C.1	A 3D print was made with magnet slots of varying radii, starting from 3 mm, stopping at 3.5 mm, and going up by (1/32) mm with each slot.	57
C.2	Slots of different sizes for holding our quarter-inch magnets were measured, and a linear relation between the slot size as modeled in CAD and the slot size as printed was found.	59
D.1	The Bokeh library allowed us to create sliders and text input for allowing the user to optimize the magnet arrangement parameters.	63

D.2	The Bokeh plot of the theoretical predicted magnetic field. The code takes a few regularly-spaced azimuthal angles and computes radial field profiles for each. In the plot, green is the mean of these profiles. Orange is the mean profile plus and minus the standard deviation of the profiles. Yellow is the maximum and minimum fields, taken from these sample profiles. The purple dots are the measured magnetic field samples from “measurements.txt,” and the thick blue are the template curves. Horizontal units are mm. This is the interactive plot that the user actually sees when changing the sliders shown in Fig. D.1. The pink rectangles are magnets below the XY-plane, the horizontal blue is the water surface, and the horizontal black is the water cell’s floor, assuming a water depth of 5 mm; the vertical units for all these objects are mm. So, this plot is the feedback part of the tool that we used to optimize for Setup-3.	66
D.3	The “magnet-arrangement.csv” file shows the arrangement parameters that can be copy-pasted to FreeCAD.	67
F.1	The FreeCAD user interface. FreeCAD is still in early stages of development, but it is quite useable and has a few features. . . .	76
F.2	The “one-ring-hole-v1” FreeCAD file has a spreadsheet with editable ring parameters.	77
G.1	We added a “Save” button to the uEye Sequencer sample program’s source code, and we used that to capture images from the camera. . . .	79
G.2	The first frame captured for each setup.	80

1 Introduction

This thesis was motivated by astrophysical accretion disks that can be found around stars and black holes. Viscosity transports momentum from one side of the disk to the other. Thus, viscosity and gravity, together, cause a Keplerian disk to form. However, viscosity is a diffusion process that would take more than a thousand times the age of the universe to form the huge disk. If the flow in the disk was turbulent, then the angular momentum transport would be enhanced. However, an instability mechanism is needed in order to make the flow turbulent. The source of the instability is yet to be determined. The disks have a Keplerian flow profile, which means that matter in the disk orbits about the center with an angular velocity $\Omega_k \propto r^{-3/2}$, where r is radial distance from the central object. While there is evidence to suggest that the Keplerian flow is stable, this has not yet been proven. The goal of this thesis was to search for an instability mechanism in the Keplerian flow itself using a table-top fluid-flow apparatus.

1.1 Accretion Disks

Accretion disks can be of different types. A black hole accretion disk is one that forms around a black hole while a circumstellar disk forms around a star. Smaller disks that rotate about neither black holes nor stars are called protoplanetary disks if they eventually form a planet. Regardless of the type of disk, the matter rotating about the central object falls into the central object and accumulates at the center: it is said to *accrete*.

Fig. 1.1 shows what we think accretion disks look like. If a star comes near a black hole, then mass from the edge of the star will be pulled toward the black hole by gravity. What happens next is suggested by the everyday experience: a basketball that rolls off a shelf will fall onto the floor, but, as it falls, it will speed up. When the ball is high above the floor, it is said to have a lot of *potential*

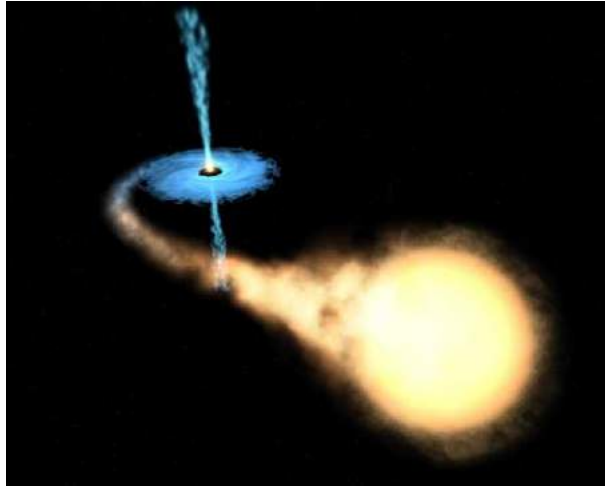


Figure 1.1: An artist’s impression of a black hole pulling matter from a star. The matter first has to orbit the black hole before it falls in. Public domain by NASA [NASA].

energy. As the ball falls, it loses this potential energy because it comes closer to the floor. Due to *conservation of energy*, if the ball loses potential energy, it must gain some other form of energy to make up for it; the other form of energy, in this case, is kinetic energy, i.e., energy of motion. Thus, the ball will speed up to make up for the lost potential energy. Matter that comes off a star and toward a black hole experiences a similar change in energy: it comes closer to the black hole into which it is falling, and, like the basketball, it makes up for the potential energy loss by speeding up and gaining kinetic energy. The total energy remains constant.

Now, it is very unlikely that the matter will be falling directly toward the black hole. Before it came near the black hole, the star was traveling along its own course, and the star’s matter also travels in the same direction as the star. When the black hole pulls on the matter, the matter starts traveling toward the black hole, but not *straight* toward it because of the matter’s inertia. The matter will “miss” the black hole, swooshing past it and not entering it. This is a typical elliptical orbit, as Fig. 1.2 shows. In any orbit, the angular momentum,

$$\vec{L} = \vec{r} \times m\vec{v}, \quad (1.1)$$

must be conserved. Here, \vec{L} is the angular momentum vector, m is the mass of the object in orbit, r is the radial position, and v is the velocity of the object in orbit. Holding a non-zero \vec{L} constant means that r can never be 0, so the object will never fall into the center unless it loses angular momentum by some mechanism.

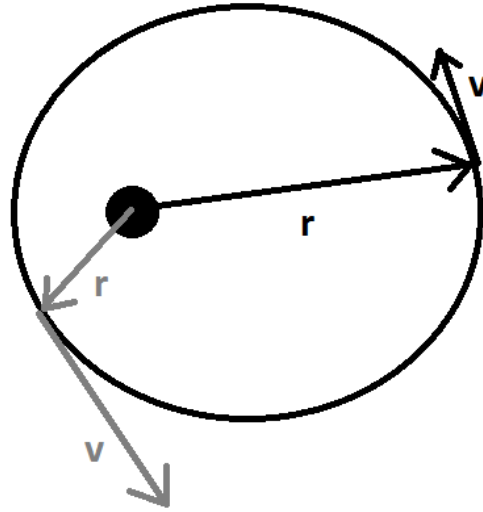


Figure 1.2: In an orbit, angular momentum is conserved. When radial position, r , is small, the velocity, v , has to be large to keep angular momentum constant.

Intuitively, water in a funnel does not go straight into the center either, unless it starts out directly towards the center to begin with. This can be seen in Fig. 1.3, where water in the funnel first makes a few rotations before falling into the center.

Both water in the funnel and accretion disks in outer space benefit from *viscosity*. If not for viscosity, this would be an endless cycle. Viscosity is a measure of the resistance of a fluid to deformation by shear. In everyday terms, a high viscosity of some liquid means the liquid is “thick,” “hard to stir,” or “hard to swim in.” Think honey. Accretion disks are not nearly as viscous as honey, but they do have viscosity, often referred to as *local* viscosity because it takes time for mechanical changes at one point in the fluid to reach another point in the fluid. Viscosity dissipates some of the energy discussed above, making these disks form and accrete. However, this process is slow and disk formation would take on the order of ten thousand times the age of the universe if local viscosity was the only source of this momentum transport [Shu92]. An instability is needed to speed up the disk formation and accretion.

For the most part, the matter that constitutes these disks is a gas. A gas is made up of billions upon billions of molecules that fly around and run into each other. This situation is depicted in Fig. 1.4. Scientists refer to this idea of molecules flying and bouncing as *kinetic theory*. If the gas molecules run into each other, then they can exchange energy. In kinetic theory, the molecules’ bounces



Figure 1.3: Before coming to the center, water in a funnel first rotates due to inertia and conservation of angular momentum; matter in an accretion disk undergoes the same process.

are treated as elastic collisions where both momentum and mechanical energy are conserved. It can be shown that one particle can lose some mechanical energy while another can gain some mechanical energy if both particles run into each other. For example, if the particles are of the same mass and they undergo a head-on collision, then their velocities will be exchanged after the collision under the classical mechanics approximation. That is, particle 1 will have a final velocity of particle 2's initial velocity, and particle 2 will have a final velocity of particle 1's initial velocity. Thus, any momentum that particle 1 had is now carried by particle 2. If particle 2 then bumps into a particle 3, it will pass on the momentum from particle 1 to particle 3.

The discussion of kinetic theory helps understand accretion disks. If a one-dimensional chain of particles is imagined, it can be seen from the discussion above that eventually the momentum from particle 1 can be transported all the way to the end of the particle chain. Accretion disks are three-dimensional, but the idea applies: momentum transport is when the faster-moving gas particles closer to the central object pass on their momentum to the outer particles. This momentum transport slows the inner particles down, so they can fall into the central object. In an accretion disk, the matter *rotates* instead of moving in a linear fashion, so in accretion disk terms, the *angular* momentum is transported outwards.

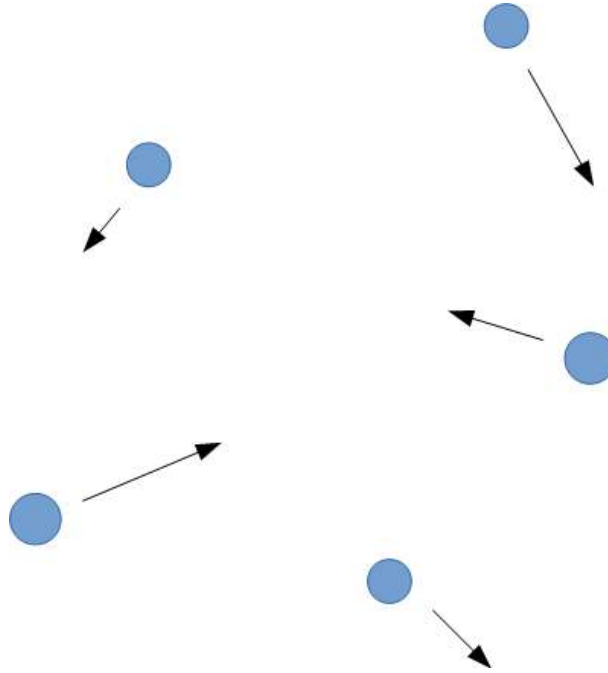


Figure 1.4: In kinetic theory, molecules fly around and run into each other, exchanging kinetic energy.

However, there is a source of controversy. Accretion disks are believed to be made up of low-density (“thin”) gas, which has low viscosity. Viscosity is a diffusion process because particles randomly run into each other, and accretion disks are huge. The amount of time diffusion takes scales as the diffusion object’s length squared, so accretion disks being huge means that the time it takes for them to form and accrete is *very* huge. In fact, it has been shown that an accretion disk would take approximately 3×10^{14} years to form if this diffusion process was the only cause of angular momentum transport [Shu92]. To explain the actual lifetime of accretion disks, which is about seven to eight orders of magnitude less than this huge lifetime predicted by kinematic viscosity alone, theoretical astrophysicists who run accretion disk simulations use an additional correction term called an *anomalous viscosity*. This thesis does not focus on simulations, but it is still important to think about the source of this anomalous viscosity. The source of the anomalous viscosity is likely turbulence, which can enhance mixing and transport [Wei51], but the instability that causes this turbulence is not well understood, as will be discussed in Section 1.3.

If we only include viscous effects, accretion disks are predicted to have a Keplerian velocity profile. This means that the gas in the disks moves in the same pattern of motion as planets move around the Sun, and slowly spiraling inward.

In the case of a fluid, the velocity field is the relation between the position in the fluid and the velocity (speed, direction) at which the fluid is moving at that point. The velocity profile is the relation between the velocity and the radial position. While there are other proposed instability mechanisms, as discussed in Section 1.3, this thesis aims to answer the question: can the turbulence be caused by purely hydrodynamic instabilities of the Keplerian flow profile itself?

1.2 Experimental Setup

The goal of this thesis was to establish a table-top model of Keplerian flow. We established the flow by electromagnetically driving it. We put salt water into a tray sitting in a magnetic field. As seen in Fig. 1.5, the tray had copper electrodes; we connected the terminals of an electric power source to these electrodes in order for electric current to go through the water. An electric current inside a magnetic field causes an electromagnetic force, so our water began to move when we turned on the power supply. By accurately shaping the magnetic field with magnets, we could achieve Keplerian forcing, as discussed in Chapter 3. We create the magnetic field by arranging magnets in circles, as in Fig. 1.6. The water tray is called a *cell* (tray with electrodes), and it is placed on top of the magnet tray, as in Fig. 1.5. Thus, if this water cell sits on top of the magnet tray, then adjusting the vertical positions of the magnets relative to the water will enable us to adjust how strong the magnetic field is at different spots on the surface of the water, which in turn will allow us to adjust the velocity profile of the water layer, described next in Chapter 2.

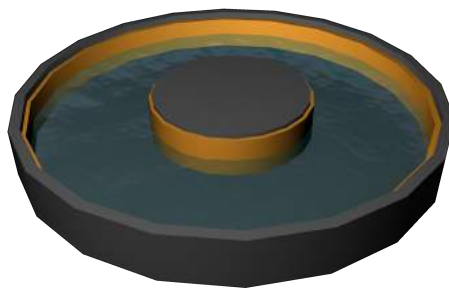


Figure 1.5: A water cell that has cylindrical symmetry can be used to drive a circular water flow. There are copper electrodes (the “circular pieces of metal”) touching the water: one in the center, and one on the outer wall.

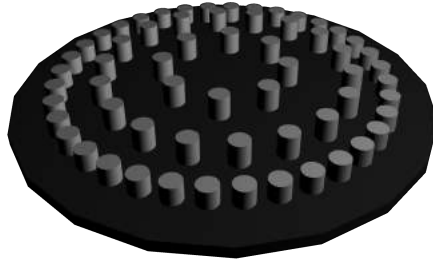


Figure 1.6: An array of magnets arranged in a special way can create our desired magnetic field profile.

The other details of the setup were: we put a camera above the cell, added small floating glass bubbles into the water to visualize the flow, adjusted the forcing to create a Keplerian flow, and analyzed the recorded video on a computer to see if we can find turbulence and characterize any instability mechanisms. The details of the experimental setup are described in Chapter 3.

1.3 Research Context

The literature has explored possible mechanisms of angular momentum transport in astrophysical accretion disks. Turbulence and local viscosity is one idea, but there is evidence against purely-hydrodynamic turbulence [Haw95; JBSG06; KB07; Hos15; SJBG12]. Hawley has investigated numerical simulations of various transport mechanisms: global (turbulent) instabilities, spiral shock waves, tidal instabilities, and magnetohydrodynamic (MHD) turbulence [Haw95].

Magnetohydrodynamics is the hydrodynamics of electrically-conducting fluids. A magnetic field can induce electric currents in moving fluid, and the currents can change the magnetic field. MHD is much better than local viscosity at coupling the motion of particles of fluid that are very far away from each other. For a conducting fluid, such as salt water or a plasma, MHD can cause turbulence and enhance momentum transport.

Hawley has argued that the transport mechanism, just like the transport itself, must be generic. According to Hawley, it thus must be MHD turbulence for every disk because MHD turbulence was the mechanism that worked the best in the simulations [Haw95]. MHD turbulence is caused by magnetorotational instability

(MRI). MRI arises when two electrically-conducting fluid elements are tethered magnetically to each other; if the disk has a decreasing angular velocity as a function of radial position, then the fluid element closer to the disk center will tug on the outer fluid element, giving it some of its angular momentum. Thus, fluid elements may remotely transfer angular momentum to each other without coming into physical contact. Thus, the criteria for MRI is a radially decreasing angular velocity, which is exactly what the Keplerian profile does [Haw95]. Ji et al. investigated a Keplerian flow in a Taylor-Couette cylinder and concluded that angular momentum transport due to purely-hydrodynamic turbulence is too inefficient for astrophysical disks, indirectly supporting the MRI mechanism even for cold disks [JBSG06]. If a disk has ionization or gas in the form of plasma, then the disk is said to be *hot*; otherwise, the disk is *cold*. There is no significant ionization for a cold disk, but Ji suggests that MHD turbulence can still happen.

The evidence supporting MHD turbulence is not conclusive, however. Despite the argument that Ji et al. give [JBSG06], they do not explain in their paper how MRI can happen for cold disks; they simply state that it is the most likely candidate based on more arguments that they give. However, cold disks are not likely to have significant effects from MHD turbulence because they do not have significant amounts of ionization. Without ionization, they cannot couple to external magnetic fields that would drive instabilities and cause turbulent mixing and transport angular momentum efficiently. Some kind of hydrodynamic effect is thus still a viable candidate for the angular momentum transport mechanism [LO10; BRS12]. Lesur and Ogilvie proposed that vertical convection is responsible for angular momentum transport in cold disks [LO10]. Belyaev et al. explored momentum transport due to acoustic modes in the boundary layer between the disk and the star it circles [BRS12]. The boundary layer is where the accretion disk meets the surface of the star. Kratter and Lodato reviewed the role of gravitational instability (GI) in the angular momentum transport process in circumstellar disks [KL16]. Kratter and Lodato suggested that GI may be the dominant transport mechanism for cold disks that are massive, while MHD may be the dominant transport mechanism for hot disks.

However, all authors either looked at Keplerian flows through simulations or experimentally investigated them in a Taylor-Couette system; none of them experimentally studied the Keplerian flow profile in detail. This thesis aims to use particle image velocimetry (PIV) along with a setup similar to the one used in [KO11] to search for purely hydrodynamic instabilities of Keplerian flow. Keplerian flow may be stable; there is analytical evidence [Ste75], and evidence from simulations [GL99; HBW99]. My experiment is important because 2D Keplerian flow has not been investigated experimentally before. Regarding accretion disks, we hope my results suggest one of the transport mechanisms to be more likely than

others. If either GI or MHD turbulence is required for efficient transport, and if my experimental setup accurately reflected the viscosity of astrophysical disks but only lacked the self-gravity and extreme heat that real astrophysical disks have, then there would have been no significant turbulence or instability found in the data. In other words, I will not have found efficient momentum transport in my setup if GI or MHD is required for the momentum transport to take place in real astrophysical disks.

A limitation in the experiment was my lab’s ability to create an accurate reflection of viscosity-related properties that are in real astrophysical disks: whereas real disks have viscosity but no edge effects, lab experiments take place in an imperfect cell and are prone to experimental error. For example, my fluid may have been too viscous, or my water cell may have been too rough, or the edges may have played such a role that they caused Ekman effects. Ekman effects are “secondary flows induced by nonoptimal axial boundary conditions,” and they have misled previous experiments [SJBG12]. They are expected to be absent from real astrophysical disks [SJBG12]. Thus, due to such experimental error factors, I expected to possibly see turbulence in my experiment even if there should not have been turbulence, had I had all the conditions as in real astrophysical disks. That was a limitation of my experiment. However, it was still an important experiment because the velocimetry data made an interesting analysis. If I did manage to reduce these error factors to the point that I did not see turbulence from just local viscosity, then my results would have confirmed the results of Ji et al. [JBSG06]. In fact, after conducting the experiments, I found no instability in Keplerian flow. In my case, I may or may not have the same conclusion as Ji because, contrary to what Ji argues, there is more to the story than just MHD turbulence.

In Chapter 2, I discuss the mathematical and physical background necessary to design the experiment and analyze the data. Chapter 3 then describes the experimental design itself. Chapter 4 presents and discusses my results.

2 Background

2.1 Astrophysical Accretion Disks

It is believed that stars accumulate matter using accretion disks. Matter falling into a star will first fall into an elliptical orbit around the star, forming a disk. Then the matter that is nearest the star will come in contact with the star, and become part of the star. The process is called *accretion*. Stars are so far away that the details of accretion disks cannot be resolved through telescopes directly, but there is indirect evidence for their existence [LX97]. In this thesis, the existence of accretion disks is not questioned, but we want to find the mechanism by which angular momentum transport is enhanced in these disks; this mechanism is still not understood.

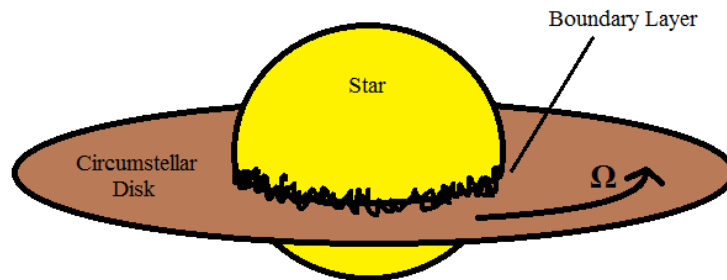


Figure 2.1: An accretion disk can be modeled as a thin disk whose matter orbits at an angular velocity $\Omega(r)$ [Shu92].

Accretion disks consist of a thin gas and small solids in orbit, but, other than a small correction due to a pressure gradient, both gases and solids in an accretion disk travel in the same Keplerian velocity profile [KL16]. Thus, I will use a gaseous disk approximation in this discussion.

An accretion disk is not necessarily thin; it can be toroidal [Haw95]. However, for the purposes of this discussion, we will assume that the disk is approximately two-dimensional and that the density of the gas is low. A model of a thin disk is shown in Fig. 2.1. This approximation holds as long as the thermal speed u_{rms} of the gas in the disk is much less than its orbital speed $r\Omega$, i.e. $u_{rms} \ll r\Omega$ where r is the radial cylindrical coordinate [Shu92]. The thermal speed can be understood by thinking back to the discussion on kinetic theory from Chapter 1. In kinetic theory, particles in a gas are constantly flying around, and their root mean square velocity can be shown to be

$$u_{rms} = \sqrt{\frac{3RT}{M}}, \quad (2.1)$$

where R is the ideal gas constant, T is the temperature of the gas, and M is the molar mass of the gas (see section 5.8 in Tro [Tro11]). Shu has used the condition that the thermal speed is small compared to the orbit of the disk around the star, i.e., $r\Omega \gg u_{rms}$, to ignore the thickness of the disk, because the characteristic vertical height is $H = u_{rms}/\Omega$ for the disk [Shu92]. Thus, the disk is considered to be thin, and $H \ll r$ holds.

For most of the disk, the angular velocity of the orbiting gas decreases outwards in a Keplerian velocity profile. Near the star, however, there is a region called the *boundary layer*, where the velocity decreases inwards. There, the angular momentum is transported from the disk to the star [PC13]. Dissipation of the gas kinetic energy creates high temperatures at this boundary layer and emits high-frequency radiation [Shu92]. In the analysis below, we ignore the boundary layer, but it is useful vocabulary for the reader who will go explore the literature after reading this thesis.

2.2 Keplerian Velocity Profile

Let us now derive the Keplerian profile. An accretion disk can be modeled as a thin disk in cylindrical coordinates (r, ϕ, z) . With $z \approx 0$ (thin disk), and with the mass of the disk much less than that of the central object, centrifugal balance can be shown, in the radial force per unit mass,

$$r\Omega^2 = \frac{GM}{r^2}, \quad (2.2)$$

where $r\Omega^2$ is the centripetal acceleration, and GM/r^2 is the gravitational acceleration of an object due to the central object of mass M a distance r away [Shu92].

Here, G is the gravitational constant. This satisfies Kepler's third law and gives the Keplerian angular velocity profile [Shu92; KL16], as

$$\Omega_k = \sqrt{\frac{GM}{r^3}}, \quad (2.3)$$

which can also be expressed more generally as

$$\Omega_k \propto r^{-3/2} \quad (2.4)$$

for any Keplerian fluid flow.

2.3 Lorentz Force

Our experimental apparatus makes use of the Lorentz force to drive a Keplerian fluid flow. For a continuous charge distribution, the Lorentz force density is

$$\vec{f} = \rho \vec{E} + \vec{J} \times \vec{B}, \quad (2.5)$$

where \vec{f} is the force density, ρ is the charge density, \vec{E} is the electric field, \vec{J} is the (electric) current density, and \vec{B} is the magnetic field. In our experiment, where we have an electrically-neutral electrolytic solution, the net charge is zero, so we may safely drop the ρ term.

The quantity $\vec{J} \times \vec{B}$ may be calculated by noting that \vec{J} is the current per unit area through a surface. If we assume that the current leaving the cylindrical electrodes of our system is uniformly distributed over the fluid layer, then this area is the cylindrical electrode's surface area that touches the fluid. If the fluid's thickness is z , then the current density is

$$\vec{J} = \frac{-I \hat{r}}{2\pi r z}. \quad (2.6)$$

Here, we used the negative sign in front of I to denote that the electric current flows from the larger-radius electrode to the smaller-radius electrode, in the $-\hat{r}$ direction. Assuming the magnetic field is directed strictly in the \hat{z} direction, the quantity $\vec{J} \times \vec{B}$, and therefore the force density as a function of r , becomes

$$\vec{f}(r) = \vec{J} \times \vec{B} = \frac{IB(r)}{2\pi r z} \hat{\theta}. \quad (2.7)$$

Finally, we can solve for the magnitude of the magnetic field if we know the force density needed. It will be

$$B(r) = \frac{2\pi rz}{I} f(r). \quad (2.8)$$

If the forcing is small, in a damped fluid flow, the velocity of an infinitesimally-small fluid element should be directly proportional to the force density of the net force on the element because the time-dependent terms of the Navier-Stokes equation will be negligible [Pur77]. We let A_p be the proportionality constant, just so we can determine a numerical value later in the experiment. Then Eq. 2.8 becomes

$$B(r) = \frac{2\pi rz}{A_p I} v_\phi(r) = \frac{2\pi rz}{A_p I} (r\Omega(r)) = \frac{2\pi z}{A_p I} r^2 \Omega(r), \quad (2.9)$$

where we have used that the azimuthal velocity, v_ϕ , is equal to $r\Omega$ for uniform circular motion, r is the radial position, and Ω is the angular velocity. This is a very important result because it shows that the angular velocity at any point in a thin layer of conducting fluid in cylindrical symmetry can be finely controlled simply by adjusting the magnetic field strength as a function of radial position. For a Keplerian angular velocity, $\Omega_k = A_k r^{-3/2}$, where A_k is some proportionality constant. With this knowledge, Eq. 2.9 becomes

$$B(r) = \frac{2\pi z A_k}{A_p I} r^{1/2}. \quad (2.10)$$

The constant A_p is a physical constant for our setup, and it has units $\frac{\text{mm}^3 \text{ rad}}{\text{A G s}}$. Its value may be found empirically. The constant A_k , on the other hand, is a control parameter, with units $\frac{\text{mm}^{3/2} \text{ rad}}{\text{s}}$; we may adjust A_k arbitrarily to control our flow's velocity scale.

In the next chapter, we describe how we went about designing and building a system with the magnetic field profile shown in Eq. 2.10. We will look at the experimental specifics, such as magnet size and type, and describe how we took velocimetry data on fluid in the system.

3 Methods

We designed three magnet arrangements, and we called them *Setup-1*, *Setup-2*, and *Setup-3*. However, we built and tested only Setup-1 and Setup-3 because the second was too complicated to 3D-print and to build. In this chapter, we will begin by describing Setup-3 and why it is important. Then we will describe our data collection procedures. Finally, we will finish by noting that we had also built Setup-1 and our reasons for it.

3.1 Design of Setup-3

As described in Chapter 1 and Chapter 2, the experiment used magnets and the Lorentz force to drive a water current. However, the magnets needed to be held in place, the parts needed to be centered, and other considerations needed to be made. This chapter describes Setup-3.

The setup needed to drive a disk-shaped fluid flow, partly mimicking the shape of accretion disks. To drive the flow, we used permanent magnets to create a magnetic field with a square-root profile, as Eq. 2.10 tells us it needs to be a square-root profile. In order to create the desired magnetic field, a collection of permanent magnets were carefully positioned using 3D-printed parts. In Fig. 3.1, it can be seen how the parts come together for Setup-3. The parts were printed on a LulzBot Taz 6. The material used was black ABS filament.

Setup-3 was a little more efficient than Setup-1 with the amount of work and building materials used to make it. Making Setup-1's rings in Fig. 3.10 keeps the magnets in place, but it also adds to the bulk of the magnet rings - it makes them take up too much space. They take up so much space that a smooth field profile is only possible at weak magnetic fields, such as the 60 gauss that we used as the maximum for Setup-1. That is, when the magnets are far away from the

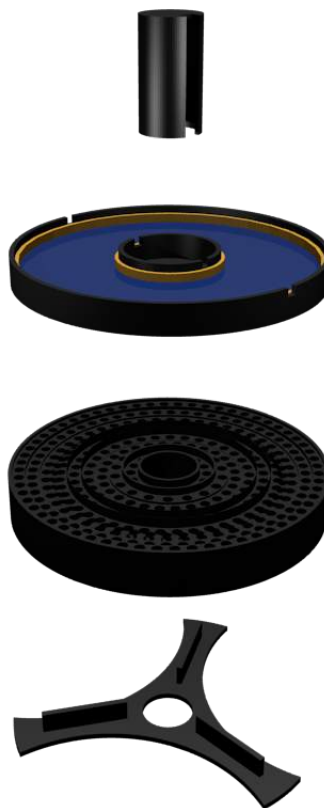
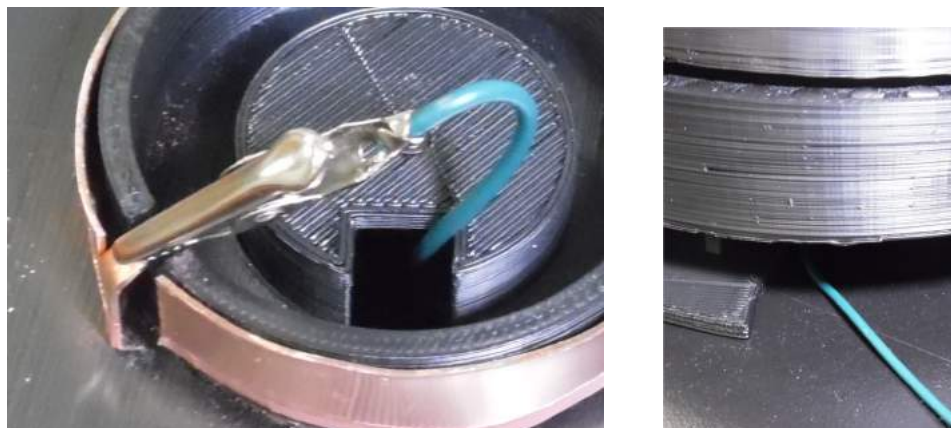


Figure 3.1: An assembly drawing of Setup-3. At the bottom is a stand that holds up a tray with a magnet arrangement. This magnet arrangement creates a magnetic field at the surface of the water in the cell sitting on top of the magnet tray. A cylindrical part centers the system.

water, their individual contributions are small, so at the water's surface the field is smooth. The discreteness of the magnets is not as apparent from the field when the magnets are that far. At the same time, the A_k constant's value is small as well in that case - the overall flow has to be very slow. Our N42 magnets could do much better than that. Instead of these removable rings, Setup-3 was crafted such that the magnets were reversibly *stuck* in the magnet tray, which was our mechanism for preventing the magnets from jumping out on their own. As discussed in Appendix C, 3.31 mm holes provided a sufficiently tight fit to hold the magnets in.



(a) Inner electrode alligator clip

(b) Alligator clip's wire

Figure 3.2: The alligator clip wire goes under the setup, through the cylinder, and onto the electrode.

There was a centering mechanism, as partly seen from Fig. 3.1. Each part in Setup-3 was made such that its inner radius is 18 mm. As the centering mechanism, a cylinder with a height of 60 mm was printed. 3D-printed parts are difficult to fit into each other, so its radius was set to just under the parts that it centers, being 17.5 mm. A notch was created in the center cylinder so that a wire can be run through it without obstructing the camera's view as shown in Fig. 3.2.

Secondly, the tray at the top should be noted. It holds our electrolyte solution. The electrodes lined the inner and outer wall of the water tray, and the electrodes were connected to the power supply using alligator clips. A camera was situated above the water tray. One problem considered was that these alligator clips, being attached to the electrodes, could obstruct some of the camera's view of the water. In order to prevent this obstruction, the tray's inner and outer walls had windows in them for specially-cut pieces of the copper electrodes to stick out of. As a result, the alligator clips could be attached from the very inside of the inner cylinder and the very outside of the outer cylinder; they did not interfere with the camera's view of the water, as seen in Fig. 3.2a.

The magnet tray itself was all one big part in Setup-3, as seen in Fig. 3.3. See Appendix E for details on the magnet arrangement. An important structural feature of the magnet tray was the *rescue holes*. These are holes that connect the bottom of the magnet slots to the bottom of the magnet tray. These rescue holes can be seen as the thin tunnels in Fig. 3.3. The holes have a radius of 1.5 mm,

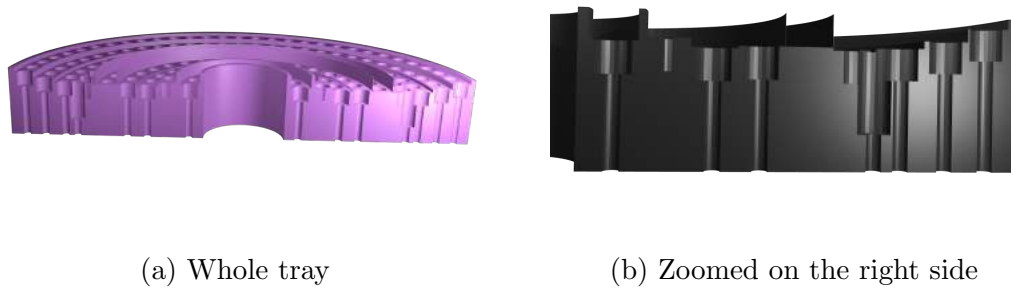


Figure 3.3: Setup-3 magnet tray cross section. The magnets are inserted by pushing down on them from the top, and they do not stick out on the top when pushed all the way in. To take them out, the “rescue holes” can be used to push them out with a thin rod. The rescue holes go all the way to the bottom of the magnet tray.

just about half a magnet radius. When it is time to take the magnets out, a thin rod can be poked into these holes to force the magnets to come out. Thus, these holes allow us to help magnets that are stuck.

3.2 Magnetic Field

The magnetic field due to many magnets is not trivial to find analytically and calculate by hand. However, by making a simplifying assumption of the magnets behaving like point dipoles, we were able to obtain results accurate enough to work for our experiment. The magnetic field due to a point dipole is defined as

$$B_x = 3Mxz/r^5, \quad (3.1a)$$

$$B_y = 3Myz/r^5, \quad (3.1b)$$

$$B_z = M(3z^2 - r^2)/r^5, \quad (3.1c)$$

where x , y , and z are cartesian coordinates, r is the distance from the origin, and the magnetic dipole is oriented up and positioned at the origin [NASb]. Appendix B reports our magnetization constant M . Using Eq. 3.1, we could calculate the approximate magnetic field due to a single magnet. We wanted to arrange magnets in rings, so we had to write Python code that took ring parameters rather than magnet parameters. The code summed over the magnetic field contributions from each magnet within each ring of magnets, and it obtained a grid of x , y , and z Cartesian components to the net magnetic field. This way we were able to plot

predicted magnetic fields before actually building each setup. For the complete Python code, see the download link in Appendix D.



Figure 3.4: We measured the magnetic field at different distances from the center for Setup-3 using a gaussmeter and a few tools that we custom 3D-printed for positioning the magnetic field probe accurately.

After building Setup-3, we wanted to know if the magnetic field physically present in our system matched the magnetic field we predicted. To measure the magnetic field, we needed a mechanism of positioning the probe. First, we 3D-printed the three-legged piece shown in Fig. 3.4. Its center also has a hole with a radius of 18 mm, so the centering is consistent. Each leg has a pocket in the shape of our gauss meter probe, 6 mm wide and 2 mm deep. The pocket was designed such that its bottom surface matched our target water level. The gaussmeter probe was placed in this pocket.

The next task was to find a mechanism for accurately positioning the probe radially, as the probe was able to slide radially inside the pocket. We designed and printed spacers of width 6 mm and of varying lengths, which came in 2.5 mm, 5.0 mm, 10.0 mm, 20.0 mm, 40.0 mm, and 50.0 mm. To position the probe at any given radial position, we placed spacers, the sum of the lengths of which adds up to that radial position minus 18 mm, against the centering cylinder. We then placed the gauss meter probe against these spacers, and held it down flat against the floor of our probe track. The measurements were obtained and plotted in Fig. 3.5. For some reason, the M constant needed to be scaled down by 80% in order to make the theoretical prediction fit the measured profile.

We have also plotted the predicted magnetic fields in Fig. 3.6. They show

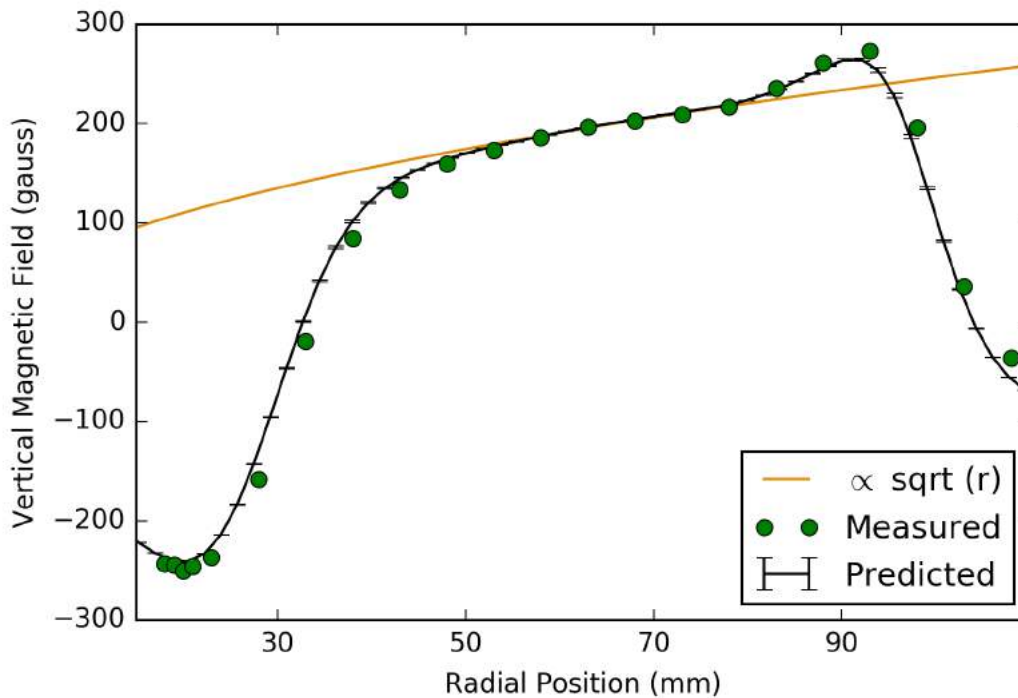


Figure 3.5: The black curve is the theoretically predicted magnetic field profile for the Setup-3 magnet arrangement. Orange is a fit to show that it is roughly square-root shaped, and green dots are measurements using a gaussmeter.

that the magnetic field in the radial direction is small for the radial positions from 50 mm to 70 mm, and that in the azimuthal direction is negligible. The vertical component of the magnetic field is the most significant component. As seen in Fig. 3.5 and Fig. 3.6, we have successfully predicted the magnetic fields and designed magnet arrangements for the specific field profile, which was the point of this section. In the next sections, we describe how we went about driving the fluid flow and measuring it.

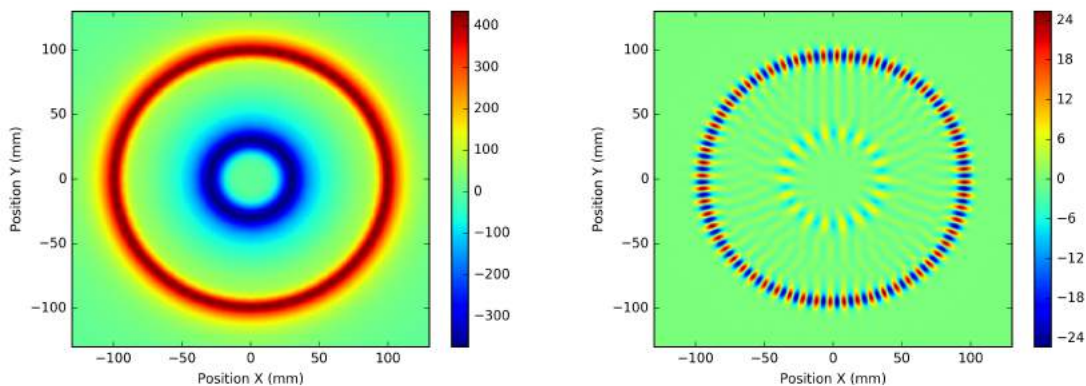
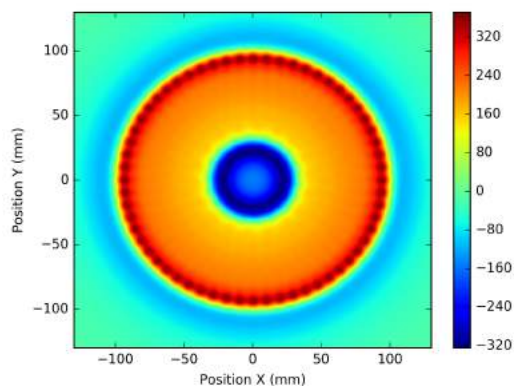
(a) Radial, B_r (b) Azimuthal, B_t (c) Vertical, B_z

Figure 3.6: The radial, azimuthal, and vertical components of the predicted magnetic field, in gauss, in cylindrical coordinates for Setup-3.

3.3 Conducting the Experiment

After we printed the parts shown in Fig. 3.1 and inserted magnets in the appropriate orientations into the slots, we made electrodes for the water cell. We cut out copper shim stock to have a width of approximately 1 cm, and we made its length be enough to fit around the wall they are lining. The result is shown in Fig. 3.7.

To record a 2D fluid flow, we needed to put the setup together. We used

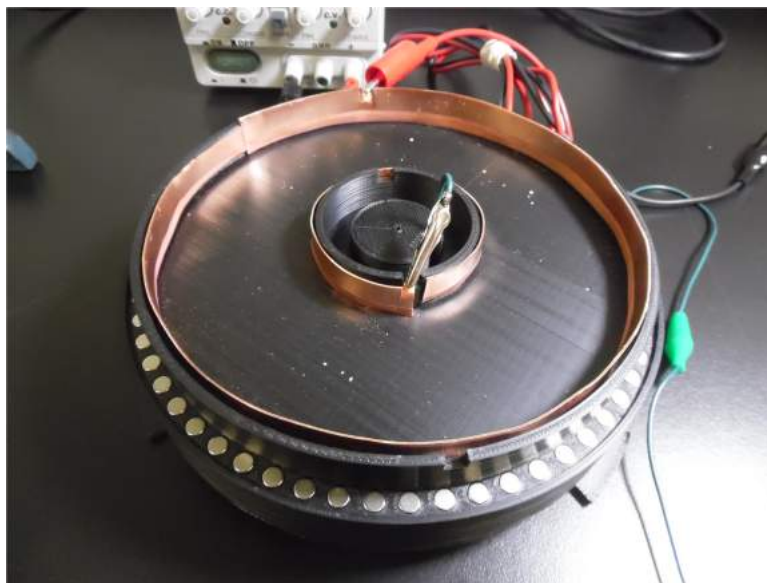


Figure 3.7: The Setup-3 system: a magnet tray, with a cylindrical water tray sitting on top of it.

113.1 mL of 1.0 M $\text{CuSO}_4 \cdot 5\text{H}_2\text{O}$ (one molar copper sulfate pentahydrate) as an electrolyte. We seeded the solution with cospheric glass bubbles.

The experimental setup is shown in Fig. 3.8. We connected a DC power supply to the electrodes and drove a current through the system. We measured the current with an ammeter, which had three decimal places of precision.

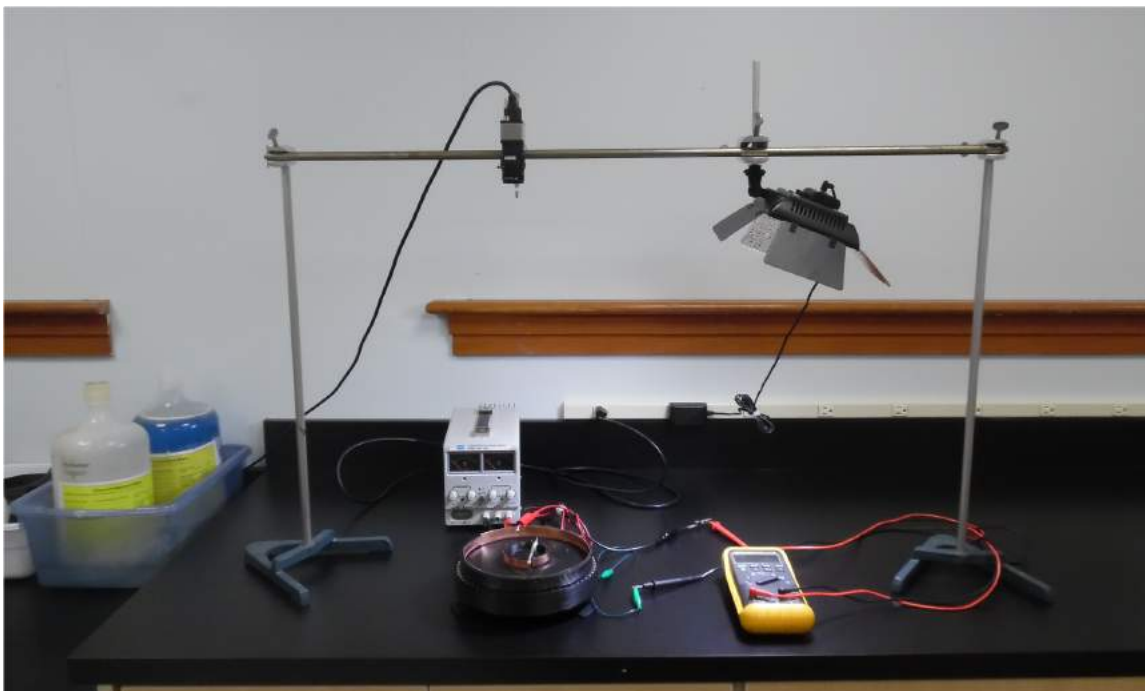


Figure 3.8: Experimental setup. There is an IDS uEye camera fixed above the system, a grid of LED lights fixed next to it, a current driver hooked up to the system, and an ammeter to monitor the current accurately.

3.4 Setup-1 as a Test

While Setup-3 was our primary experimental apparatus, it was not the first one we built. First, we built *Setup-1*, which was a prototype as well as a test to make sure Eq. 2.9 works. We chose to build Setup-1 with a field profile $\propto r^{-1.5}$. An assembly drawing is shown in Fig. 3.9.

Setup-1 was built with the thought in mind that magnets tend to align themselves anti-parallel to the magnetic field in their environment. Strong magnets will force themselves out of any magnet-holding slots that do not hold them in place tightly enough. Thus, in fear of the slots not being tight enough, we 3D-printed special rings that had not only magnet slots but also shim-stock slots for holding the magnets in the magnet slots, and we secured the magnets using specially-cut copper shim stock bars into these 3D-printed rings as shown in Fig. 3.10. Like Setup-3, rings in Setup-1 also had rescue holes. The rings were placed onto special stands for them in the bottom part of Fig. 3.9, and the setup was assembled as shown in Fig. 3.11.



Figure 3.9: An assembly drawing of Setup-1. The magnet tray is a complex part with removeable rings of magnets. The water cell sits at the top as usual.

While the resulting magnet arrangement for Setup-1 may not have been the global optimal arrangement, it yielded a quite accurate magnetic field profile. The predicted magnetic field for Setup-1 is shown in Fig. 3.13. Fig. 3.13c shows the magnetic field, B_z , in the vertical direction for Setup-1, predicted using the M and the code discussed above.

After building Setup-1, Fig. 3.12, we wanted to make sure that the magnetic field in the physical setup matched the design field. We borrowed a gaussmeter from the Kleinert lab and measured the magnetic field at various distances from the center of the setup (see Fig. 3.14). The gaussmeter provided us with magnetic



Figure 3.10: A test magnet ring with cylindrical slots for five magnets. The ring also has flat slots for copper shim stock to go through and hold the magnets in place. In case the magnets get stuck, there are small holes on the opposite side for pushing the magnets out with a thin tool. The magnets were inserted with the north (N) pole directed vertically *up*.



(a) Magnets uncovered. (b) Magnets covered. (c) Water cell on top.

Figure 3.11: Top-down view photos of the system. The magnets are inside the rings where the copper shim stock pieces are; the shim stock pieces are for holding the rings in place, as well as for preventing any magnets from jumping out.

field data, but unfortunately it was difficult to position the probe accurately to measure the field profile. Setup-1 did not print out correctly: it printed to be a little bit slanted. Plus, we were using a caliper to measure approximate radial positions of the gauss meter's probe. As a result of both of these, the B_z data for Setup-1 had millimeters of uncertainty. Nevertheless, the results were still informative.



(a) Top-front perspective.

(b) Front perspective.

Figure 3.12: Perspective-view photos of the system.

Those results are plotted in Fig. 3.15. The black curve is the field profile predicted by the method above. It comes with error bars representing the standard deviation of the profile as the various azimuthal directions are sampled. For Setup-1, the magnetic field profile varies very little with change in azimuthal direction. We wanted to see that our actual magnetic field present was indeed Keplerian, and we saw from this plot that it was, within measurement error, at least until about 85 mm or so from the center.

Despite the success of Setup-1, it had two major problems. First, it was made by a computer, namely by the `minimize ()` function. The code often returned non-physical results. For example, it would often overlap two magnet rings in space when requested to solve for a stronger magnetic field. And while not overlapping the magnets, it did not always solve for a state vector that caused a smooth profile. The target field we had it solve for had a maximum of 60 gauss at position $r = 30$ mm. However, setting this maximum even to 70 gauss made the curve not quite fit the $r^{-3/2}$ Keplerian profile. The computer could only solve for a smooth and *weak* field profile, and the problem with such a weak magnetic field was that we were not able to drive a very fast fluid flow, even when driving 5.0 A of current through the electrodes. The second major problem with Setup-1, however, was that the magnetic field should have been a square-root profile to drive a Keplerian fluid flow, by Eq. 2.9. We found the mistake after we ran the experiment and found that the angular velocity profile was actually $\propto r^{-7/2}$ rather than the desired $\propto r^{-3/2}$. That result was in agreement with Eq. 2.9, of course, but it meant we had to build another setup.

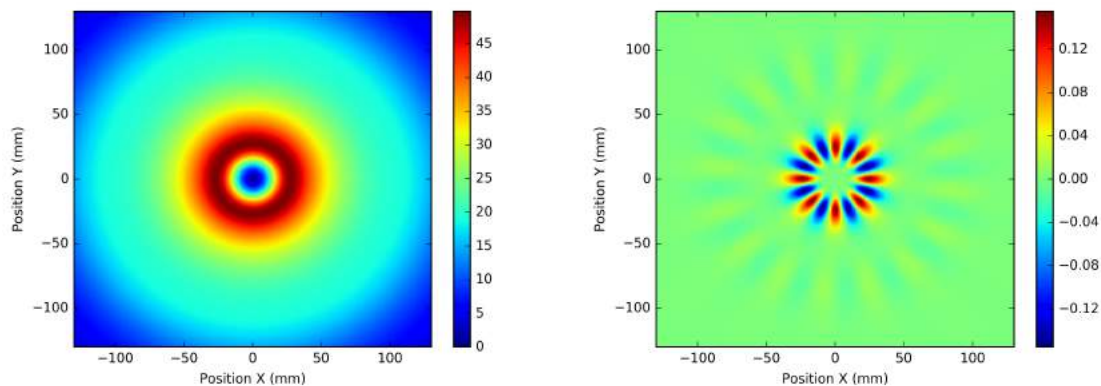
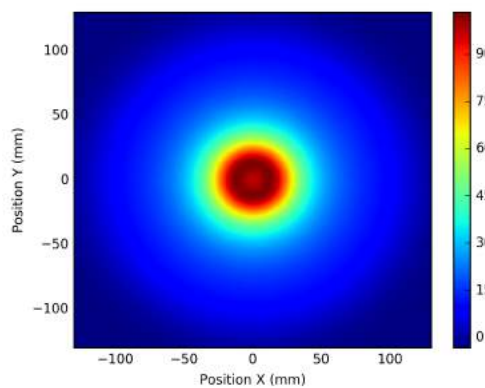
(a) Radial, B_r (b) Azimuthal, B_t (c) Vertical, B_z

Figure 3.13: The radial, azimuthal, and vertical components of the predicted magnetic field, in gauss, in cylindrical coordinates for Setup-1.

A large magnet ring holder tray was printed as shown in Fig. 3.16. For the specifics of the models, see the FreeCAD files, but the main idea is that the magnets were positioned in exactly the positions that the Python code optimized to, and the water cell had enough space for a 5 mm layer of water, with inner radius of 30 mm and outer radius of 90 mm.



Figure 3.14: We measured the magnetic field at different distances from the center for Setup-1 using a caliper and a gauss meter. The gauss meter was carefully taped to a plastic piece of width 4.5 mm, almost the 5 mm for the water level, and placed on top of the water cell's floor for measuring.

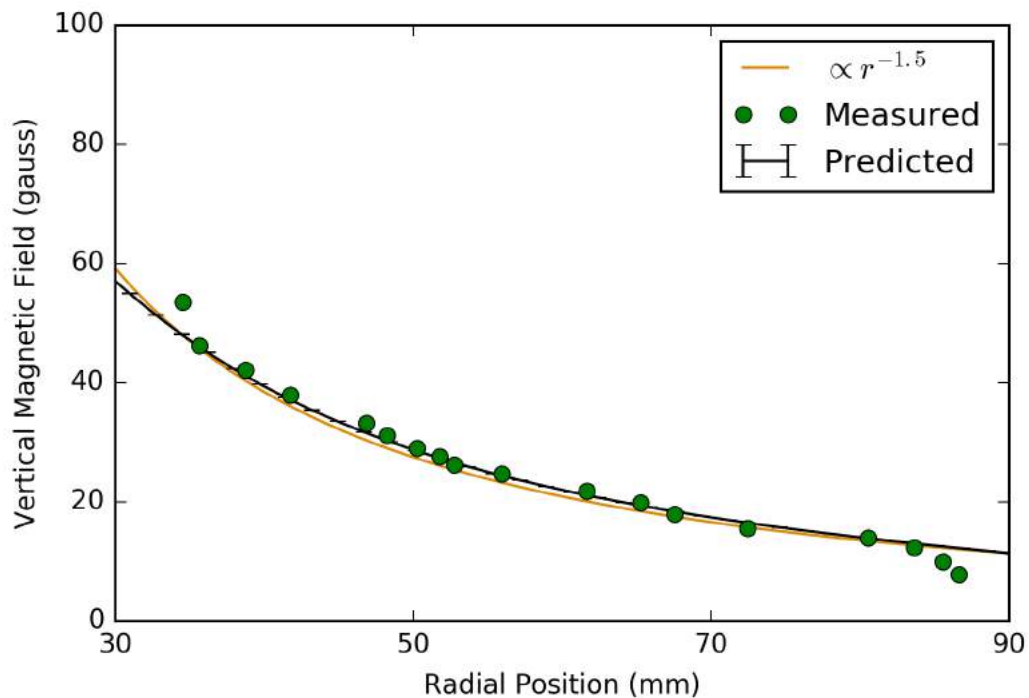


Figure 3.15: The vertical component, B_z , magnetic field profile as a function of radial position for Setup-1. The green dots are the measurement samples from the actual measurements done on the system we built, as measured by the method in Fig. 3.14. The orange line is a $r^{-3/2}$ curve scaled to fit the green dots.

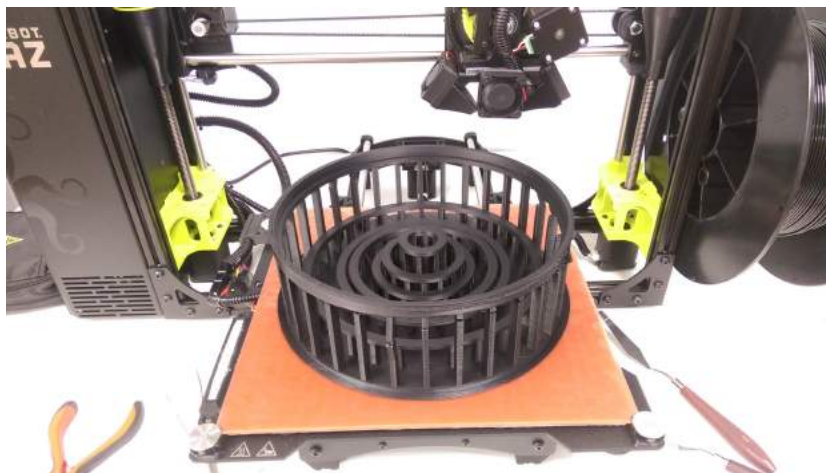
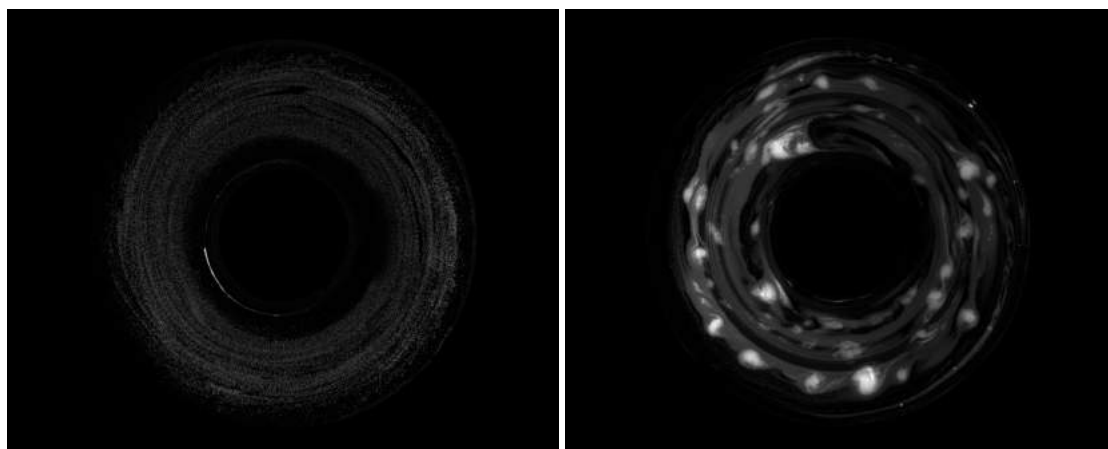


Figure 3.16: The bottom part: the magnet tray; some of the outer-most posts broke a little during printing, but it mostly turned out fine.

3.5 Taking and Processing Image Data

The next step was to record image data. We used a USB 3 uEye CP Rev. 2 camera with a HR F1.4/12 mm objective. See Appendix G for details and instructions on recording video. For best results in particle image velocimetry (PIV), the image data needed to be pre-processed before being fed into the PIV algorithm. As the first step, we decided that background subtraction would help eliminate some misleading PIV cross-correlations. A common approach is to use the statistical mean frame as the background, but we decided on the statistical minimum instead in order to avoid negative pixel values, which for unsigned integers underflow and become 256 plus the negative value; the math becomes more complicated than we would like to deal with. Changing from unsigned integers to floating-point values for the pixels could be a possible solution, but, depending on the integer size, the integer approach can take less memory, so we left it as is but used the frame with all statistical minimum pixels instead.



(a) Setup-1

(b) Setup-3

Figure 3.17: The frames after subtracting the background and filling unimportant pixels with zeros.

We subtracted the background, which was the minimum. However, slight lighting variations have caused the background to still faintly appear in this difference frame. We needed the background to not appear at all, so we found where the center pixel was in the frames of each image set, as well as how many pixels from that center the water starts and ends, and we set all the pixels outside of that range to zero. The result is shown in Fig. 3.17, which we fed to the PIV algorithm.

The next task was to find a library for particle image velocimetry (PIV). As of the writing of this thesis, there were a few libraries for MATLAB, but only

one easily-accessible library for Python, called OpenPIV. OpenPIV is also, as of this writing, not very developed yet, many features being not yet implemented; however, it works on Python - which is free and open source - and it has the most important functions developed already, such as velocimetry and validation. We settled on OpenPIV.

The OpenPIV code was run, and its local median validation methods were invoked using u and v thresholds of 2 mm/s for the `validation.local_median_val()` function. For each velocity sample, the local median method finds the median of the nearby velocities, and it takes a difference of this local median with the velocity sample under question. If the difference is greater than the specified threshold, then the velocity sample is invalidated (replaced with NaN). The (x, y) values do not change for each frame of the image sequence, but the (u, v) values could. Our fluid's flow profile appeared to be mostly constant over the time period spanned by all the frames, so we averaged all the valid (u, v) values to obtain an average (u, v) field.

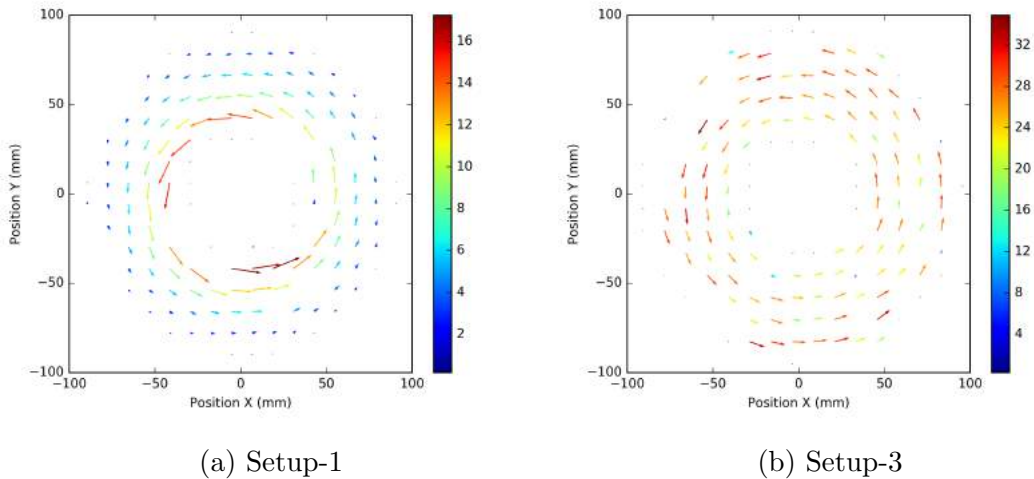


Figure 3.18: Velocity field of validated vectors.

We converted the (x, y) (position) and (u, v) (velocity) data from pixels to millimeters by using OpenPIV's scaling function, `scaling.uniform()`; we passed the ratio of pixels to millimeters to this scaling function. Thus, the average frame (x, y) was in millimeters, and (u, v) (omitting the *avg* subscript for brevity) was in millimeters per second. The result is shown in Fig. 3.18. Note, the result in Fig. 3.18 is centered. We needed to find the velocities' positions relative to the *center* of the cylindrical flow, as that greatly impacts the accuracy of finding the velocity profile. We manually entered the center pixel's position within the frame into the

code, but the code then adjusted this to minimize the radial velocity components.

We had the code do this by using the SciPy Optimize library's `minimize` () function. The scalar function we passed to `minimize` () took a 2D vector representing the center position, in millimeters, and it computed a scalar that represented how close this position is to the center of the cylindrical fluid flow. It did this by first converting the (u, v) Cartesian velocity into a radial velocity. Let \vec{r} be the position of a PIV data sample, and $\frac{d\vec{r}}{dt}$ be its velocity. Then, to convert from Cartesian coordinates to the radial cylindrical coordinate,

$$\left(\frac{d\vec{r}}{dt}\right)_r = \left(\frac{d\vec{r}}{dt}\right) \cdot \hat{r} = \left(\frac{d\vec{r}}{dt}\right)_x \hat{x} + \left(\frac{d\vec{r}}{dt}\right)_y \hat{y}, \quad (3.2)$$

where $\hat{x} = x/\sqrt{x^2 + y^2}$, $\hat{y} = y/\sqrt{x^2 + y^2}$, and \vec{r} is the (x, y) vector from PIV minus the given candidate vector for the system's center. The function passed to `minimize` () took this field of $\left(\frac{d\vec{r}}{dt}\right)_r$ values, squared them, and averaged the result. This was the scalar that was minimized to make sure that the $\left(\frac{d\vec{r}}{dt}\right)_r$ is as close to zero as possible (circular motion only, no radial component).

As another validation step, our main script took the resulting center from the above procedure multiplied the mean square value by a validation parameter to obtain a threshold,

$$v_{thr} = P_{thr} \left\{ mean \left(\left(\frac{d\vec{r}}{dt} \right)_r^2 \right) \right\}, \quad (3.3)$$

where we have somewhat arbitrarily chosen $P_{thr} = 0.5$. The script invalidated all (u, v) entries whose radial velocity, $\left(\frac{d\vec{r}}{dt}\right)_r$, was found to be greater than this threshold velocity. After that, to ensure the best accuracy, the center position was recalculated with the new, validated velocity field, using the SciPy Optimize `minimize` () procedure again.

The $\left(\frac{d\vec{r}}{dt}\right)_r$ field is shown in Fig. 3.19. As can be seen, the validation has done a nice job of ensuring that the data correctly represents a circular flow, with little radial motion.

As a next step towards finding the angular velocity profile, we needed to find the azimuthal component of the (u, v) field in cylindrical coordinates. We did that using

$$\left(\frac{d\vec{r}}{dt}\right)_\theta = \left(\frac{d\vec{r}}{dt}\right) \cdot \hat{\theta} = \left(\frac{d\vec{r}}{dt}\right)_x (-\hat{y}) + \left(\frac{d\vec{r}}{dt}\right)_y (\hat{x}), \quad (3.4)$$

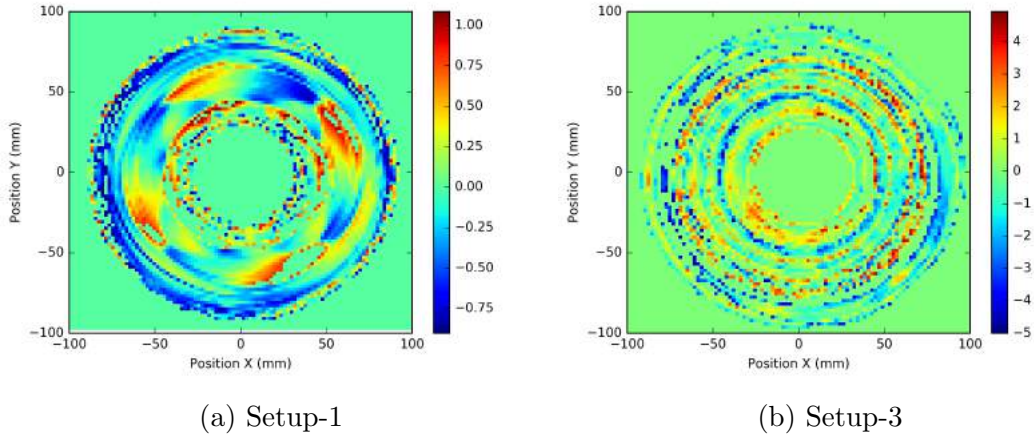


Figure 3.19: Radial velocity, $\left(\frac{d\vec{r}}{dt}\right)_r$, for each setup.

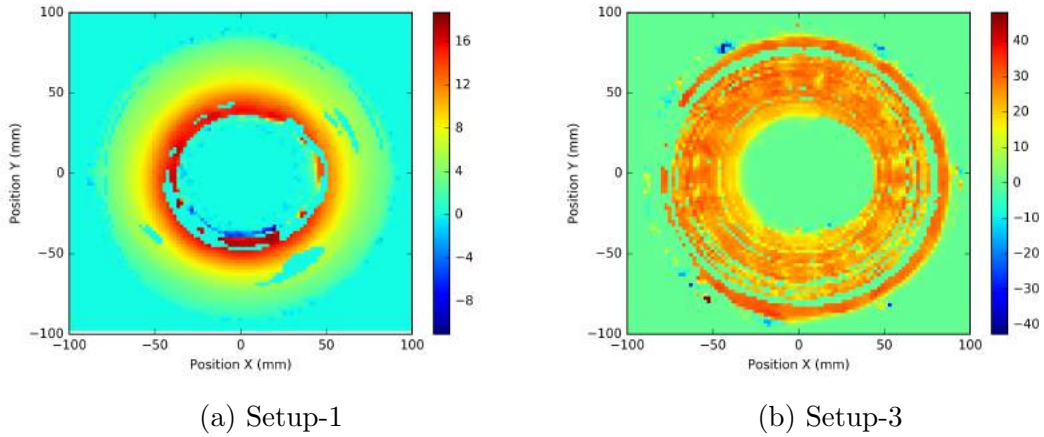


Figure 3.20: Angular velocity, $\left(\frac{d\vec{r}}{dt}\right)_\theta$, for each setup.

where we have used that $\hat{\theta} = -\hat{y} + \hat{x}$. From this, we found the $\left(\frac{d\vec{r}}{dt}\right)_\theta$ field, which is plotted in Fig. 3.20.

We needed to verify that our flow was Keplerian, so we fit our angular velocity profile to a power law. In order to do so, we started with the relation

$$\omega = Ar^P, \quad (3.5)$$

where ω is angular velocity, r is radial position, and A and P are some constants. Taking the log of both sides reveals that A and P may be found by fitting a line to the log data, as

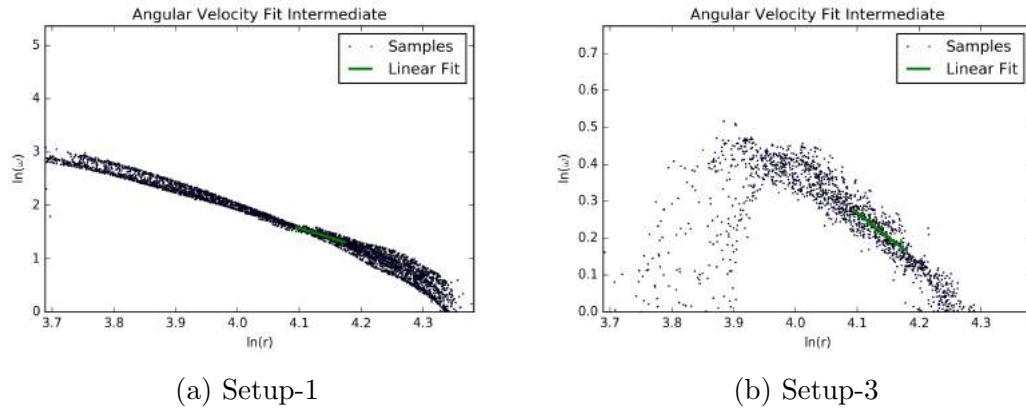


Figure 3.21: Measured angular velocity in log-space plotted with a linear regression fit.

$$(\ln(\omega)) = (\ln(A)) + (P) (\ln(r)). \quad (3.6)$$

We fit the data using P as the slope and $\ln(A)$ as the y-intercept, and we obtained the result shown in Fig. 3.21. For details on fitting lines using least squares, see Taylor, [Tay97], and Appendix H. The velocity profile results are shown in Fig. 3.22.

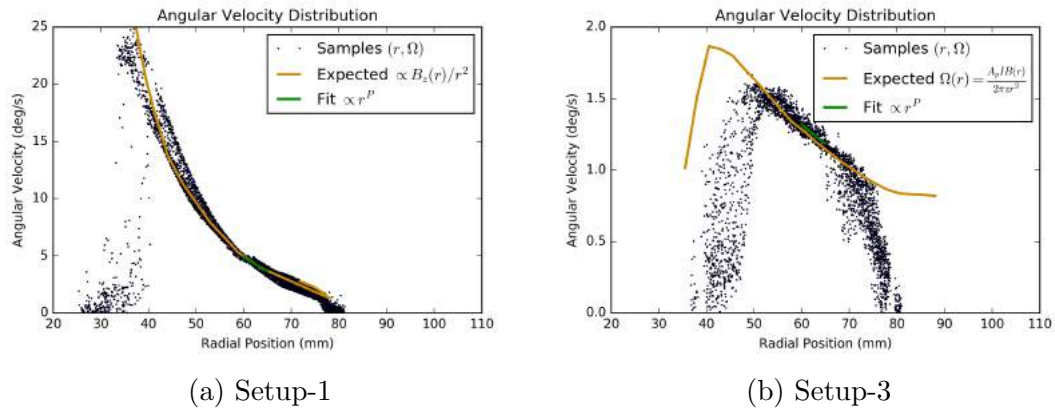


Figure 3.22: Measured angular velocity plotted with a power fit and an expected angular velocity based on Eq. 2.9 and the constant A_p found in Section 3.6.

For our fits, we fit only data within a middle radial position range because both the magnetic field and the velocity profile is complicated near the edges. We used a padding of 20 mm from either edge of the 30 mm to 90 mm water range, so our fits were between radial positions of 50 mm and 70 mm. The data and

their fits are shown in Fig. 3.22. The plot also has an expectation curve, which is based on Eq. 2.9 and the A_p value determined later in this thesis, in Section 3.6.

Numerically, for Setup-1, the fits turned out to be

$$F_A = 17.17 \pm 0.06 \quad (3.7a)$$

$$F_B = -3.69 \pm 0.02. \quad (3.7b)$$

For Setup-3, they were

$$F_A = 4.96 \pm 0.26 \quad (3.8a)$$

$$F_B = -0.43 \pm 0.06. \quad (3.8b)$$

After that, we took the same data for more electric currents, as described next, in Section 3.6, and found how our fluid flow profile behaves. This data will be presented in the next chapter. In the meantime, in Section 3.6, we find the A_p constant of proportionality from Eq. 2.9.

3.6 Angular Velocity's Proportionality Constant to the Magnetic Field

At this point in the analysis, we had many data samples of angular velocities calculated from PIV data, as in Fig. 3.22. The samples looked like $(r, \omega(r))$. They can be related to the magnetic field using Eq. 2.9 as long as the magnetic field is known, so

$$B(r) = \frac{2\pi z}{A_p I} r^2 \Omega(r) \quad (3.9)$$

where $B(r)$ is the magnetic field and $\Omega(r)$ is the fluid's angular velocity at radial position r while a current I is driven through the fluid, and the fluid's thickness is z . The only unknown left in the experiment at this point was A_p . Rearranging, we obtain

$$A_p = \frac{2\pi z}{IB(r)} r^2 \Omega(r). \quad (3.10)$$

At this point, finding A_p was trivial because it is a simple function of the known parameters. The maximum likelihood value of A_p was taken to be the mean of the

RHS of Eq. 3.10, and the uncertainty in the found A_p was the standard deviation.

For Setup-1, the current was $I = 1.0$ A, while for Setup-3 it was $I = 0.021$ A. There was more uncertainty from the PIV data itself than from the current measurements, so the current measurements were considered to be exact, without uncertainty. For both setups, the water thickness was $z = 5$ mm. The magnetic field for each angular velocity sample was taken as a linear interpolation of the data from Fig. 3.14 and Fig. 3.4, using NumPy `interp()`. Numerically, the best estimate value for A_p was

$$A_p = (561 \pm 15) \frac{\text{mm}^3 \text{ rad}}{\text{A G s}} \quad (3.11)$$

from the Setup-1 data, and

$$A_p = (645 \pm 15) \frac{\text{mm}^3 \text{ rad}}{\text{A G s}} \quad (3.12)$$

from the Setup-3 data.

We continued taking data and analyzing PIV for more electric currents. The imaging beads in the fluid began to centrifuge outward and not show up well on PIV at high electric currents, so, for Setup-3, we only considered the data for currents less than or equal to 0.5 A. We took a weighted average of the A_p samples obtained as above. For the weighted average equations, see Appendix H.

In the next chapter, we present all the high-level data from Ω (previous section) and A_p (this section).

4 Results and Discussion

This chapter presents the results from the experiments. First we show the general trends for Setup-3 in Section 4.1. Then we show examples of low-level analysis in Section 4.2 and Section 4.3. Finally, we conclude with our final thoughts in Section 4.4.

4.1 High-level trends from Setup-3

In this section, we examine the trends in Setup-3. We do this by varying the electric current and seeing how that affects the parameters found in the previous section. Namely, we are interested in the numerical value of the power in the power law fit of the angular velocity samples from PIV. This is the power part of $\propto r^P$. We are also interested in the proportionality constant, A_p .

The currents were varied between 0 A and 1 A, but the data for currents greater than 0.5 A jumped around a lot due to the imaging particles centrifuging out from the system's spinning. Thus, for the numerical findings, only data from currents of 0.5 A and less were taken into account.

For 500 mA and below, the weighted-average results are

$$\Omega(r) \propto r^{(-1.157 \pm 0.009)}, \quad (4.1)$$

for the angular velocity, and

$$A_p = (627 \pm 2) \frac{\text{mm}^3 \text{ rad}}{\text{A G s}}, \quad (4.2)$$

for the A_p constant.

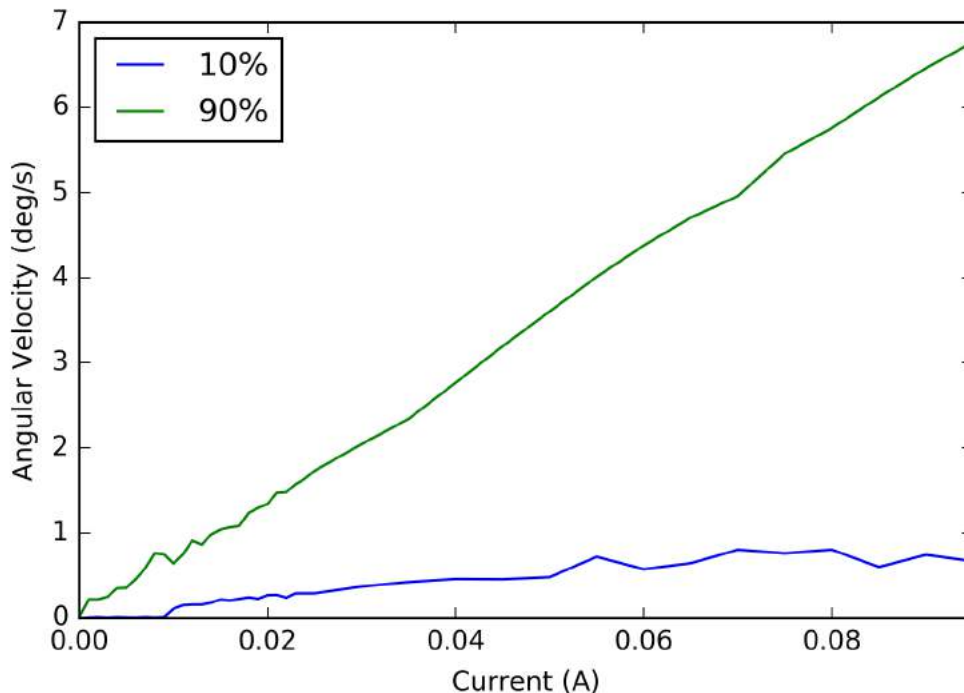


Figure 4.1: The angular velocity is proportional to the current.

In Fig. 4.1, it can be seen that the fastest 10%, as well as the slowest 10%, of the fluid has angular velocity directly proportional to the current. This is in agreement with Eq. 2.9, as expected.

The power law's power, P , is shown in Fig. 4.2. It is approximately constant, except our knowledge of it is rather uncertain for currents below 25 mA or so. This is possibly due to PIV error at such low velocities, but it may also be because of air currents in the room.

The proportionality constant fit trends are shown in Fig. 4.3. Our A_p constant is also uncertain for small currents, possibly for the same reasons as the P , discussed above. This constant's fit value becomes clear sooner than the power P , however, as its uncertainty and standard deviation drops starting at around 15 mA. Overall, because A_p is mostly constant, this data agrees with our initial derivation in Eq. 2.9.

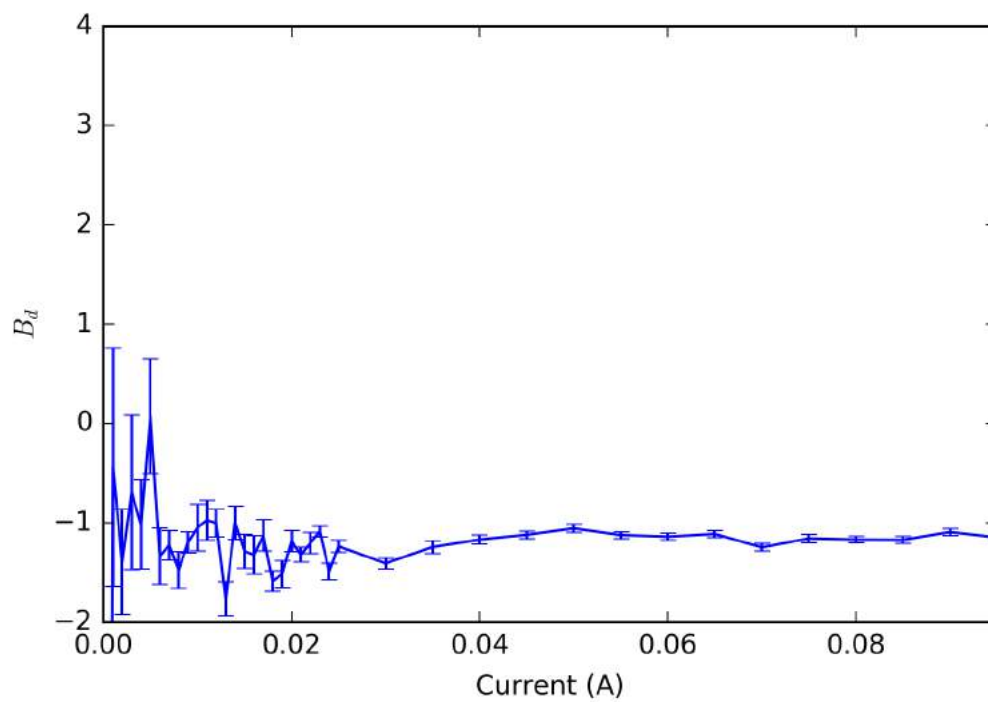


Figure 4.2: The angular velocity's power profile jumps around a lot for small electric currents but evens out to around -1.2 at larger currents.

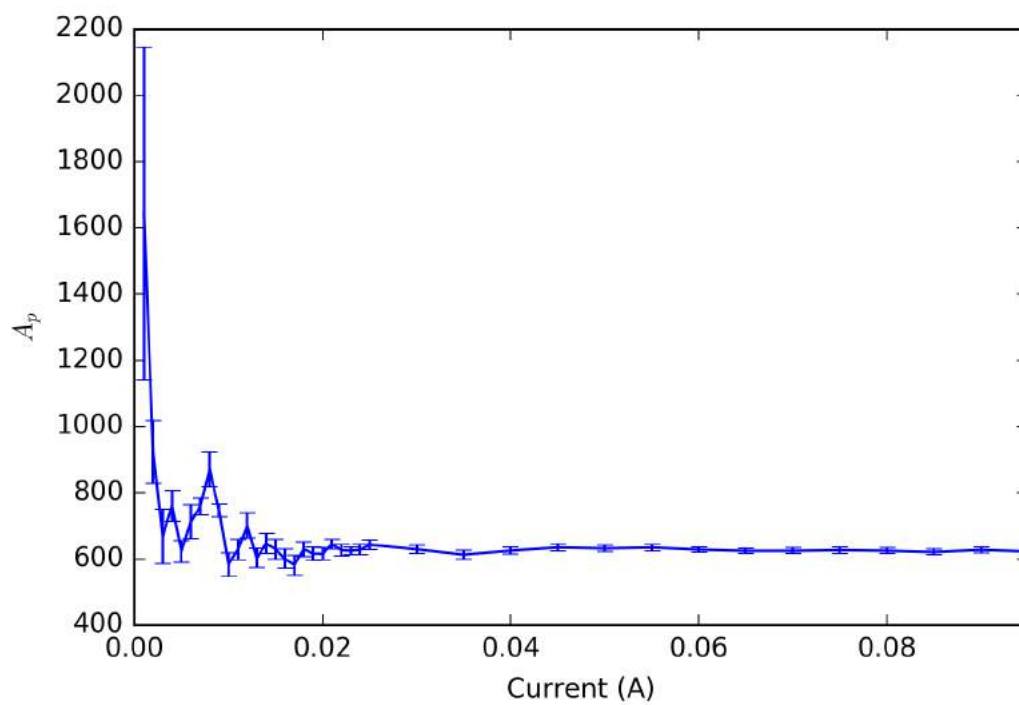


Figure 4.3: The constant, A_p , is chaotic for very small currents, but evens out starting from around 20 mA.

4.2 A snapshot of Setup-3

This section presents a snapshot of the type of data that went into the trends shown in the previous section. The $\Omega(r)$ power law and the A_p constant were found as described in Chapter 3. Data from a trial where the electric current was $I = 21$ mA is shown in Fig. 4.4 and Fig. 4.5. The angular velocity power law was

$$\Omega(r) \propto r^{(-1.32 \pm 0.07)}, \quad (4.3)$$

where $\Omega(r)$ is angular velocity at radial position r . The magnetic field for Setup-3 was designed such that it is $\propto r^{+0.5}$, so the fact that our $\Omega(r)$ power law is approximately 0.5 minus 2 is in approximate agreement with Eq. 2.9. For an estimate of how *strong* the flow is compared to the other parameters ($B(r)$, I , etc.), the A_p constant is a more reliable measure. The A_p parameter's value from this Setup-3 data was found to be

$$A_p = (645 \pm 15) \frac{\text{mm}^3 \text{ rad}}{\text{A G s}}. \quad (4.4)$$

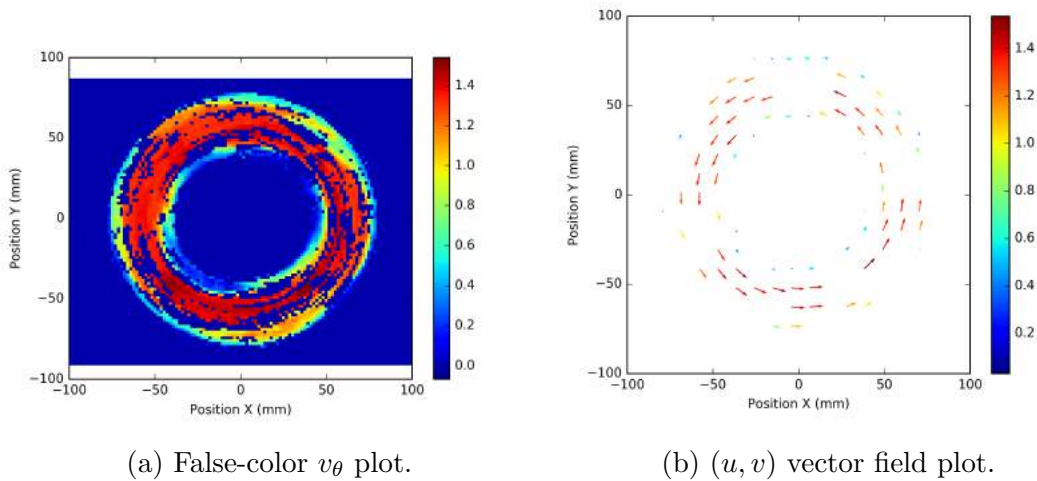


Figure 4.4: Setup-3. After the PIV analysis, vector fields were obtained representing particle velocities, (u, v) . The velocities' magnitudes, v_θ , are shown in false-color on the left, and the actual (u, v) vector field is shown on the right. The vectors are pointing mostly in the counter-clockwise direction.

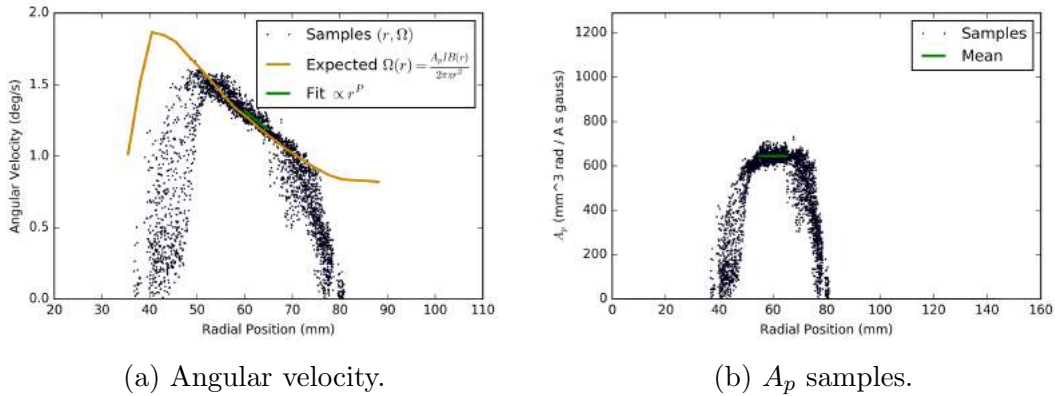


Figure 4.5: Setup-3. Left: The flattened $(r, \Omega(r))$ data (flattened means we turned the 2D data into a 1D array) was fit against a power law, $y = Ar^P$. The fit was only done on the part of the curve that fit a power law. Right: The A_p samples (see previous chapter) and their mean value as the green curve.

4.3 A snapshot of Setup-1

The data from Setup-1 was also analyzed using PIV. As discussed in the previous chapter, the velocity profile and the A_p parameter were found. Fig. 4.6 shows the average velocity field obtained from the OpenPIV analysis after validation. Fig. 4.7 shows the angular velocity profile and the A_p parameter. From the v_θ fit, the power law was

$$\Omega(r) \propto r^{(-3.52 \pm 0.08)}. \quad (4.5)$$

The magnetic field for Setup-1 was approximately $\propto r^{-1.5}$, and the $\Omega(r)$ being $\propto r^{-3.5}$ is also in agreement with Eq. 2.9. The A_p parameter from Setup-1 data was

$$A_p = (561 \pm 15) \frac{\text{mm}^3 \text{ rad}}{\text{A G s}}. \quad (4.6)$$

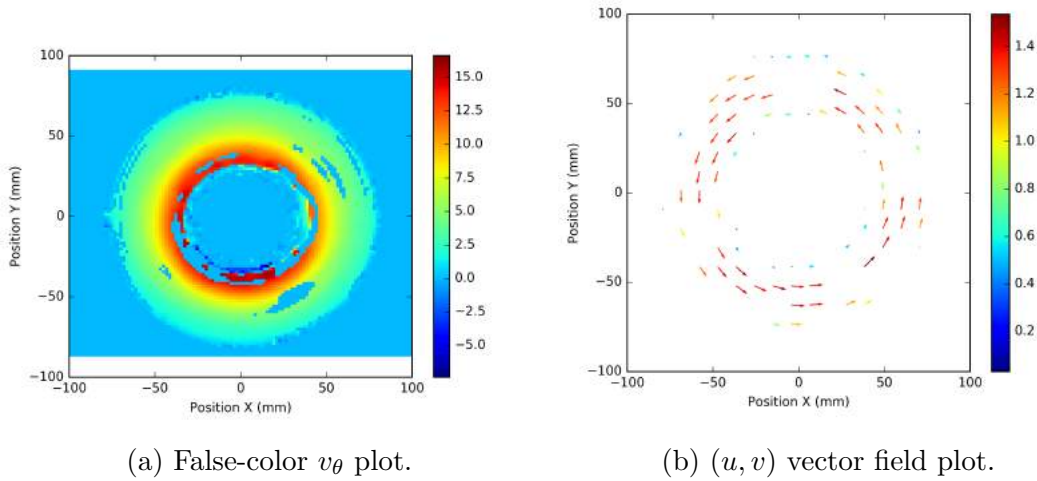


Figure 4.6: Setup-1. After the PIV analysis, vector fields were obtained representing particle velocities, (u, v) . The velocities' magnitudes, v_θ , are shown in false-color on the left, and the actual (u, v) vector field is shown on the right. The vectors are pointing mostly in the counter-clockwise direction.

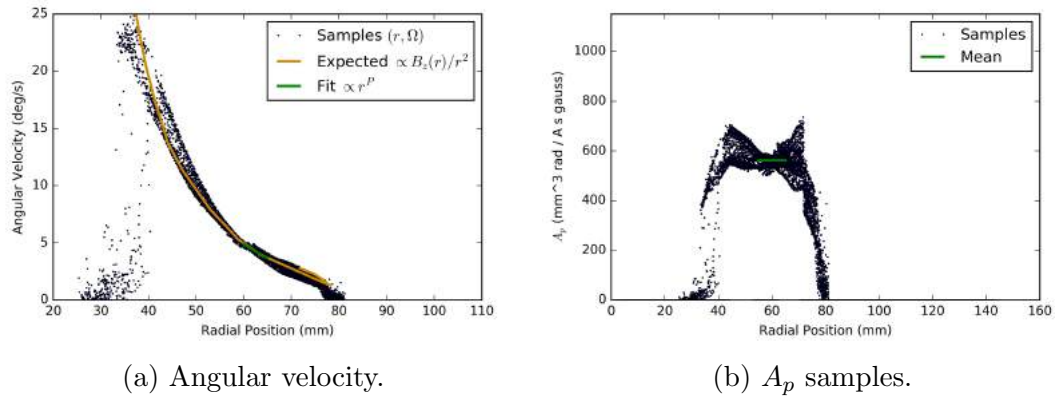


Figure 4.7: Setup-1. Left: The flattened $(r, \Omega(r))$ data was fit against a power law, $y = Ar^P$. The fit was only done on the part of the curve that fit a power law. Right: The A_p samples (see previous chapter) and their mean value as the green curve.

4.4 Final Thoughts

We built two pieces of experimental apparatus in this thesis. One had a Keplerian magnetic field, and one drove an almost-Keplerian fluid flow. No instability has been observed with this Setup-3 yet. However, the power was not quite -1.5 as expected for a Keplerian profile, so Keplerian flow will still need to be continued

to be investigated in the future.

For future experiments of this sort, we have determined the A_p constant to help with designing these fluid flows. The constant is

$$A_p = (627 \pm 2) \frac{\text{mm}^3 \text{ rad}}{\text{A G s}}, \quad (4.7)$$

and it can be used in the equation

$$\Omega(r) = \frac{A_p I B(r)}{2\pi z r^2} \quad (4.8)$$

where I is the electric current, $B(r)$ is the magnetic field at radial position r , and z is the water level in the cell.

One of the limitations, as alluded to in Chapter 1, was Ekman effects. In a system like this, fluid elements near the floor are slowed by shear, and this slowing makes the centrifugal force on those fluid elements weaker than the centrifugal force on the elements traveling faster above them. Thus, there was Ekman pumping in our system, where at the water surface the fluid was rotating and moving radially outward slowly. On the other hand, the fluid near the bottom rotated in the same direction but slowly moved radially inward. This was particularly noticeable in Setup-3 and for currents greater than 1 A. Our PIV analysis was not affected very much by this because we only focused on small currents, but a future study may be to find a fix to this Ekman pumping.

We may also make some improvements to make the angular flow more Keplerian. As it is, the center cylinder is fixed, but if it rotated with the flow, then the flow would not drastically fall off near the center. Another idea is to investigate how A_p is affected by the other parameters. The A_p is derived to be a constant, but in the real world it still varies a little with radial position. Of course, if not for the boundary conditions, A_p would probably not vary with radial position.

There were limitations to this study, but it was still informative. While we cannot make a definite conclusion about Keplerian flows, we can at least say that a flow that is close to Keplerian seems pretty stable, as we have not observed any instability in our setup yet.

Bibliography

- [Ale16] Objects Inc. Aleph, *Lulzbot taz 6 user manual*, <https://download.lulzbot.com/TAZ/6.0/documentation/manual/TAZ-6-Manual.pdf>, 626 West 66th Street, Loveland, Colorado, 80538 USA., 2016.
- [Ame91] American Chemical Society, *Safety video by american chemical society (1991)*, <https://www.youtube.com/watch?v=9o77QEeM-68>, 1991.
- [BRS12] Mikhail A. Belyaev, Roman R. Rafikov, and James M. Stone, *Angular momentum transport and variability in boundary layers of accretion disks driven by global acoustic modes*, *The Astrophysical Journal* **760** (2012), no. 1, 22.
- [Fre] FreeCAD, *Basic part design tutorial*.
- [GL99] Patrick Godon and Mario Livio, *On the nonlinear hydrodynamic stability of thin Keplerian disks*, *The Astrophysical Journal* **521** (1999), 319–327.
- [Haw95] John F. Hawley, *Keplerian complexity: Numerical simulations of accretion disk transport*, *Science* **269** (1995), no. 5229, 1365.
- [HBW99] John F. Hawley, Steven A. Balbus, and Wayne F. Winters, *Local hydrodynamic stability of accretion disks*, *The Astrophysical Journal* (1999).
- [Hos15] Masahiro Hoshino, *Angular momentum transport and particle acceleration during magnetorotational instability in a kinetic accretion disk*, *Physical Review Letters* **114** (2015), no. 6, 061101.
- [JBSG06] Hantao Ji, Michael Burin, Ethan Schartman, and Jeremy Goodman, *Hydrodynamic turbulence cannot transport angular momentum effectively in astrophysical disks*, *Nature* **444** (2006), 343–346.
- [K&] Magnetics Inc. K&J, *The K&J magnetic field calculator*, <https://www.kjmagnetics.com/fieldcalculator.asp>.

- [KB07] Zdenka Kuncic and Geoffrey V. Bicknell, *Towards a new standard theory for astrophysical disk accretion*, *Modern Physics Letters A* **22** (2007), no. 23, 1685.
- [KL16] Kaitlin M. Kratter and Giuseppe Lodato, *Gravitational instabilities in circumstellar disks*, *Annual Review of Astronomy and Astrophysics* **54** (2016), 271–311.
- [KO11] Douglas H. Kelley and Nicholas T. Ouellette, *Using particle tracking to measure flow instabilities in an undergraduate laboratory experiment*, *American Journal of Physics* **79** (2011), no. 3, 267.
- [LO10] Geoffroy Lesur and Gordon I. Ogilvie, *On the angular momentum transport due to vertical convection in accretion discs*, *Monthly Notices of the Royal Astronomical Society: Letters* **404** (2010), no. 1, L64–L68.
- [LX97] Mario Livio and Chun Xu, *On the observational evidence for accretion disks in active galactic nuclei*, *The Astrophysical Journal Letters* **478** (1997), no. 2, L63–L65.
- [NASa] NASA, *Accretion disk*, https://en.wikipedia.org/wiki/File:Accretion_disk.jpg, Public domain.
- [NASb] ———, *Properties of magnetic dipoles*, https://ccmc.gsfc.nasa.gov/RoR_WWW/presentations/Dipole.pdf.
- [Nor11] Mark J. Norton, *Using freecad*, <http://opensourceecology.org/w/images/0/00/FreeCAD-3.pdf>, 09 2011.
- [PC13] Martin E. Pessah and Chikwan Chan, *Angular momentum transport in accretion disk boundary layers around weakly magnetized stars*, *EPJ Web of Conferences* **46** (2013), 04004.
- [Pur77] E.M. Purcell, *Life at low Reynolds number*, *American Journal of Physics* **45** (1977), no. 1, 3–11.
- [Shu92] Frank H. Shu, *The physics of astrophysics: Gas dynamics*, vol. 2, ch. 7, pp. 82–92, University Science Books, 1992.
- [SJBG12] Ethan Schartman, Hantao Ji, Michael J. Burin, and Jeremy Goodman, *Stability of quasi-Keplerian shear flow in a laboratory experiment*, *Astronomy and Astrophysics* **543** (2012), A94.
- [Ste75] J.M. Stewart, *The hydrodynamics of accretion discs I*, *Astronomy and Astrophysics* **42** (1975), 95.

- [Tay97] John R. Taylor, *Introduction to error analysis: The study of uncertainties in physical measurements*, 2nd ed., University Science Books, 1997.
- [Tro11] Nivaldo J. Tro, *Chemistry: A molecular approach*, 2nd ed., Pearson, 2011.
- [Wei51] C.F. von Weizsäcker, *The evolution of galaxies and stars*, The Astrophysical Journal **114** (1951), no. 2, 165–186.

A Safety Tips

Future Borrero lab member, please read this chapter! We have put together some recommendations for being safe while working in the Borrero lab. The lab's 3D printer has burn, pinch, and cut hazards. The copper shim stock is a cut hazard. While it is not as dangerous as a chemistry laboratory, there are still chemical hazards.

A.1 3D Printer Safety

As with any device, please read the user manual before using the 3D printer. Or at least read the safety warnings on page 8! The user manual is available from [Ale16]:

<https://download.lulzbot.com/TAZ/6.0/documentation/manual/TAZ-6-Manual.pdf>

In addition, there is a hard copy of the user manual in the cabinet labeled "3D Printer."

Our main advice to the future printer user is to be really careful and watch in which direction their hands may jerk. The printer's extruder head has sharp edges that may peel the skin on one's hand off if their hand jerks and hits the printer head while attempting to take out a part that has finished printing. We remember this happening to some people, so it is a serious issue. We recommend lifting the printer head all the way up above the bed before taking a printed part off the bed. The head may be lifted by taking the following:

1. Push on the printer's user interface wheel next to the screen to open the menu.

2. Select “Movement.”
3. Select “Move Axis.”
4. Select “Move 10mm.”
5. Select “Move Z” (to move UP).
6. Spin the wheel a rotation or so to the right. This will set the Z position to 270 mm.
7. The head may take some seconds to move all the way up. Please be patient.

A.2 Metal-Cutting Safety

Projects like the one described in this thesis involve making electrodes, if not from copper than from some other metal. The copper shim stock is thick, and it may scratch the future Borrero lab student if they are not as careful as they should be. The most important advice we would give is to work around the copper shim stock carefully and semi-slowly. Watch out for the copper’s edges, which are sharp and have cut people before. Wear safety goggles, as little pieces of the metal may fly off unexpectedly.

A.3 Chemical Safety

On my first day of chemistry lab at Portland State University last summer, the lab TA was explaining the lab rules to us. One of these rules was to not bring food or drink to lab. “Is water okay?” I asked cleverly, knowing that water is almost always allowed, even if other food and drink is prohibited. “You can bring water, but you will have to leave it in a cubby near the door,” the TA responded. I learned that the lab had the rule not to keep the lab clean, but rather to keep us safe.

Fellow students, please do not bring food to the lab. The Borrero lab does not have substances that are so hazardous that they will kill a person quickly, but it does have chemicals. Vapors from chemicals may condense on the food or drink. A similar precaution may be said for makeup. If applying makeup in the lab, chemicals from the air may become trapped between the skin and the makeup.

When handling chemicals, read their safety data sheets. We have hard copies in a red folder on a shelf inside the cabinet labeled “Safety.” The safety data sheet (SDS), formerly known as material safety data sheet (MSDS), provides information about a chemical’s hazards, safety precautions, first aid measures, and much more information. These are organized into sections. For example, the “acetone” SDS starts on the first page with the hazards identification, where it says “causes serious eye irritation.” Under section 8.2, “exposure controls,” the SDS explains the personal protective equipment (PPE) necessary, which is safety goggles and gloves for acetone. Section 9, “physical and chemical properties,” lists the melting point of acetone as $-94\text{ }^{\circ}\text{C}$ and the boiling point as $56\text{ }^{\circ}\text{C}$. These are important numbers to note when reading a safety sheet because a low-boiling-point solvent will evaporate readily at room temperature and pose a hazard of being inhaled. Always close the lid after using it.

One final remark on handling chemicals. I took a near-empty bottle of acetone up to Leslie Coop for a refill one day. She refilled it for me, but instead of handing me the bottle back, she first placed it into a big plastic jar, screwed the lid onto the jar, and handed me the whole jar. “We never carry liquids without putting them into something else first,” she said, and I returned to our lab with the jar. The lesson for me was to carry liquids inside another tray or container. In the Borrero lab, there is a demo tray in the “Demo” drawer at the bottom; that may be used to conduct or carry demos with liquids. Additionally, there is a big, clear plastic jar in the far glassware cabinet. That jar may be used for placing smaller bottles into for carrying somewhere.

For more information on chemical safety, please see the American Chemical Society’s safety video [Ame91]:

<https://www.youtube.com/watch?v=9o77QEeM-68>

B Finding Dipole Magnetization Constant

To simplify magnetic field prediction, we made the simplifying assumption that our magnets behave like point dipoles. With this assumption, the magnetization constant was all we needed to start predicting the magnetic fields caused by complicated magnet arrangements. This appendix describes how we used an online magnetic field calculator to find the magnetization constant.

Before we discuss the magnetic field, first we will note that we used N42-grade magnets that were $1/4''$ thick and $1/4''$ in diameter. The strongest grade available was N52, but N42 was the best strength for the money, making it a suitable choice for us. As far as size, smaller is better if a smooth magnetic field is desired - contribution from many discrete magnets can be smoothed better than the contribution from few strong magnets. On the other hand, we had to handle the magnets by hand, so they needed to be large enough in size to be handled. We decided that $1/4'' \times 1/4''$ will be the most practical trade-off for the experiments in this thesis.

B.1 Magnetization Constant from K&J Magnetics Calculator

To find the dipole magnetization constant of our magnets, we first went to the K&J Magnetics website and found a magnetic field strength calculator [K&J]. We used it to probe different positions in space above the magnet and then performed a dipole fit on the collected data. This section tells how we arrived at the $M = (2.20 \pm 0.05) \times 10^5 \text{ Gmm}^3$ result.

Since we chose to treat our magnets as dipoles, we needed to find the dipole magnetization constant of our magnets. Conveniently, the K&J Magnetics website

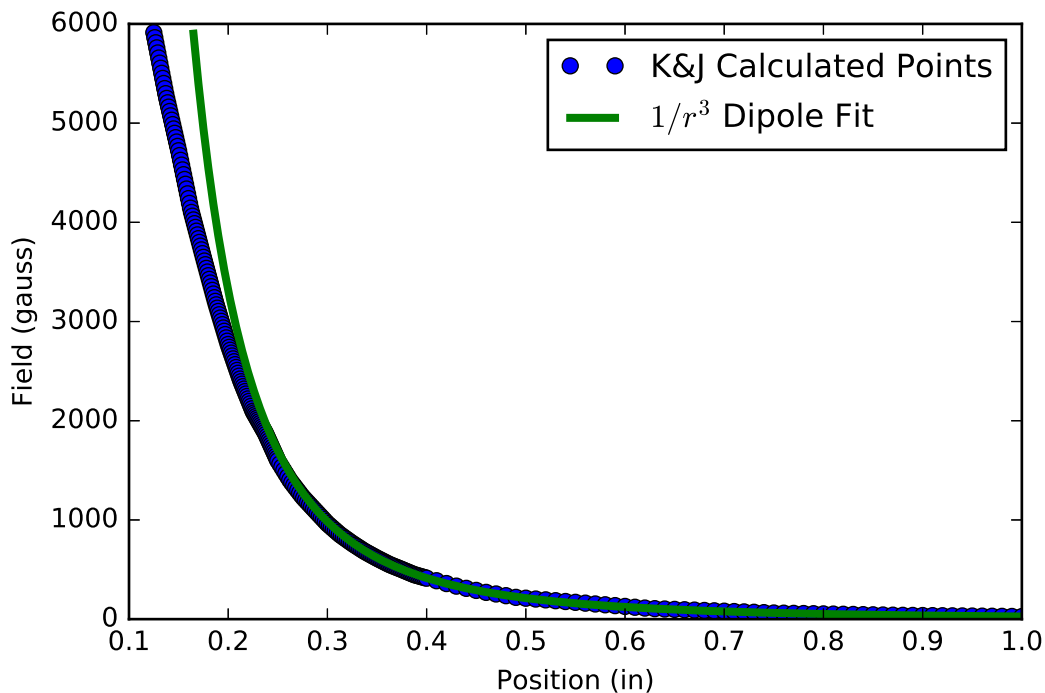


Figure B.1: Magnetic field strength calculated for our N42 $1/4'' \times 1/4''$ magnet from the K&J Magnetics website [K&J]. A magnetic dipole fit has been placed over the tail, where position is at least 0.4in from the center of the magnet. The position was measured vertically from the center of a magnet that is oriented with its north axis up.

had a magnetic field calculator for their cylindrical magnets, from which we were able to approximate this constant. Fig. B.1 shows the finite element calculations, done by K&J's magnetic-field calculator, as well as a magnetic dipole fit on the tail of the data-set. If our assumption is valid that far from the magnet the field should be approximated by a dipole, then we should be able to fit a $\propto 1/r^3$ curve on the data samples. If the curve fits the data well, it will give us an accurate estimate of the magnetic dipole moment. In the figure, the field strength is plotted as a function of vertical position above the center of the magnet. Fig. B.2 shows how well our M fits the data. The data deviates only a little from being a constant.

The magnetic field's radial component, B_r , in spherical coordinates can be written as [NASb]

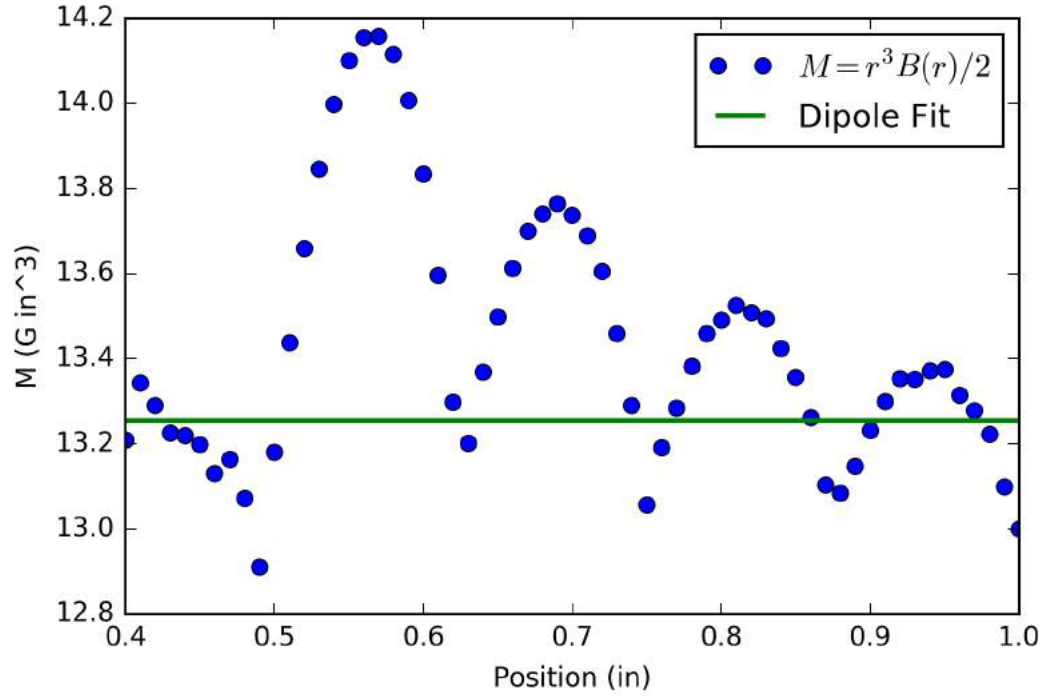


Figure B.2: The intermediate $(r, r^3 B(r)/2)$ form used to fit M , the dipole magnetization constant.

$$B_r = \frac{2M \cos(\theta)}{r^3}, \quad (\text{B.1})$$

where M is the magnetization constant of the dipole and r is the distance from the dipole center. The data in Fig. B.1 was collected for varying distances probing directly over the *top* of the magnet, i.e., 0° from the vertical. This means the spherical coordinate $\theta = 0^\circ$, and therefore $\cos(\theta) = 1$. From Fig. B.3, it can also be seen that $B_r = B_z$, where B_z is the vertical component of the magnetic field in Cartesian coordinates. Plugging these into Eq. B.1, we can simplify the magnetic field to

$$B_z = B_r = \frac{2M}{r^3}. \quad (\text{B.2})$$

This equation may be rewritten in terms of M as

$$M = \frac{1}{2} r^3 B_z. \quad (\text{B.3})$$

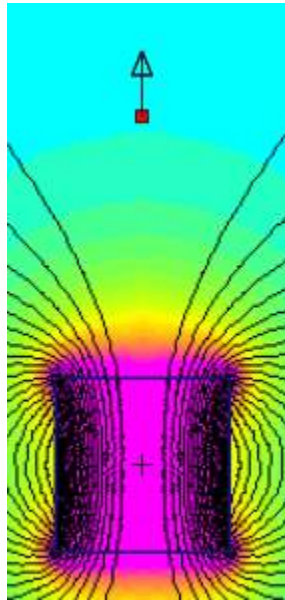


Figure B.3: The K&J Magnetics finite element magnetic field calculator was used to find the predicted magnetic fields directly above the magnet, a distance r away from its center. Image by [K&].

Again, our goal was to be able to find parameters that we can use to arrange many magnetic dipoles, such that the parameters will give us a certain magnetic field profile. If we find M for this special case where we know B_r , and where $B_r = B_z$, then we can plug the M back into the general Eq. B.1 or into one of the other equations from [NASb] to find any component of the magnetic field for any position or orientation in space. To find M , we fit a $2M/r^3$ curve over the tail of the data in Fig. B.1. The tail was chosen to be ≥ 0.4 in because that was where the curve started looking the most like $\propto 1/r^3$ when we plotted it. In other words, we used Eq. B.3 to calculate an M estimate for every data sample above 0.4 in. Then the mean and standard deviation of these M values were used as the best estimate, $M = (2.20 \pm 0.05) \times 10^5 \text{ Gmm}^3$.

B.2 Measuring the Constant from an Actual Magnet

Next, we set out to make the same measurements as in the previous section but using a gaussmeter and a real magnet. We needed a precise method of positioning the gaussmeter probe. The department has a milling machine, but we were wor-

ried about its metal parts becoming magnetized and affecting the magnetic field. Therefore, we 3D printed plastic parts to serve as a probe positioning mechanism.

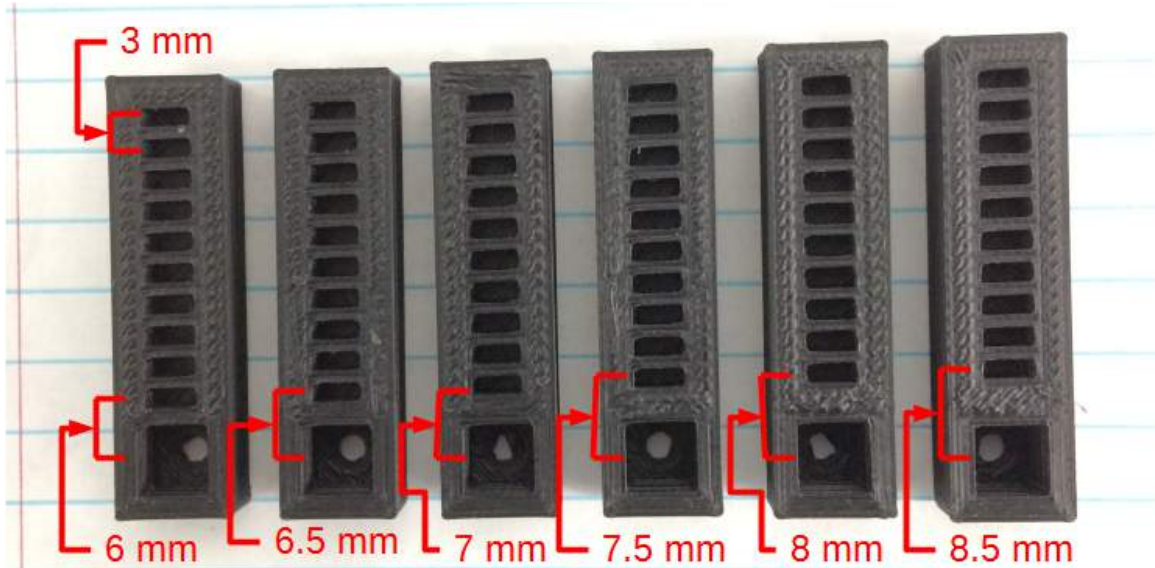


Figure B.4: We designed and printed six rulers for accurately placing our gaussmeter probe at known positions above a magnet. The slots are spaced such that the slots' centers are 3 mm apart.



Figure B.5: The slots were just a little bit too big, so we put tape around the probe and magnet in order for them to fit perfectly.

The parts we made are shown in Fig. B.4 and Fig. B.5. We printed six of these *rulers* that had 10 gaussmeter probe slots each, spaced 3 mm apart from each other. The first ruler's first gaussmeter probe slot was 6.0 mm above the center of the magnet slot, and this first slot position increased by 0.5 mm for each consecutive ruler, as the labels describe in Fig. B.4. This way, we were able to measure the magnetic field at positions in increments of 0.5 mm, starting from 6.0 mm and ending just before 36.0 mm.

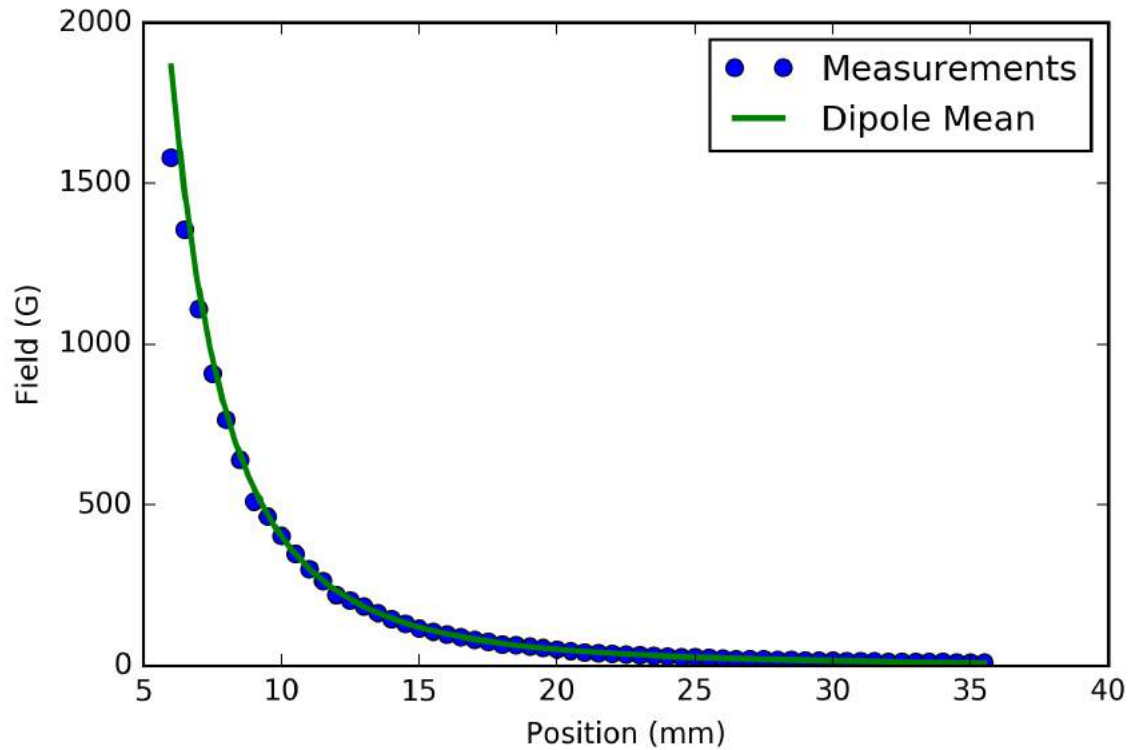


Figure B.6: Magnetic field strength measured for our N42 $1/4'' \times 1/4''$ magnet using the Kleinert lab’s gaussmeter. The position was measured vertically from the center of the magnet.

To find M from these, we used the same procedure and Eq. B.3 as in the previous section. The results are shown in Fig. B.6 and Fig. B.7, and the numerical result was $M = (2.01 \pm 0.09) \times 10^5 \text{ Gmm}^3$. The difference between this result and that of the previous section is approximately $(0.19 \pm 0.14) \times 10^5 \text{ Gmm}^3$. The 0.19 is only slightly larger than the uncertainty, 0.14, in the difference, so the discrepancy is not large between the two M values. Thus, the numerically-calculated M from the previous section was used in all the code for this project.

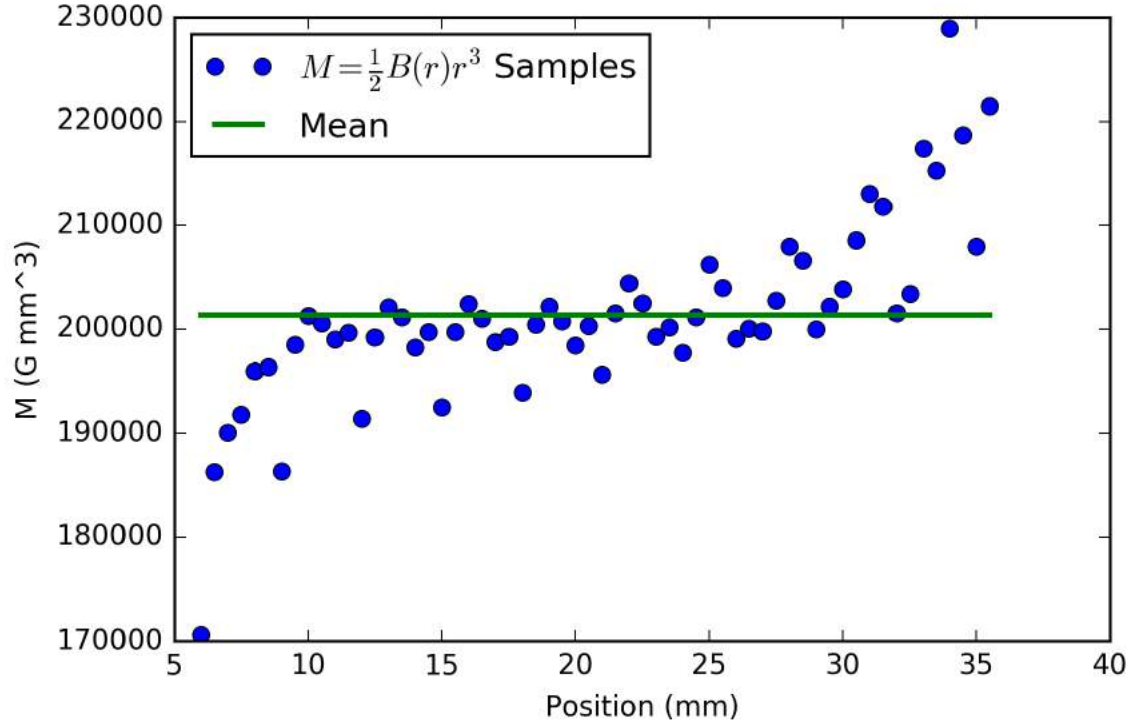


Figure B.7: The intermediate M form (Eq. B.3) used to fit the curve in Fig. B.6.

B.3 Using the Dipole Magnetization Constant

At this point, having a numerical value for our M , we were in a position to be able to calculate the magnetic field for any magnet arrangement using the following equations

$$B_x = 3Mxz/r^5, \quad (\text{B.4a})$$

$$B_y = 3Myz/r^5, \quad (\text{B.4b})$$

$$B_z = M(3z^2 - r^2)/r^5, \quad (\text{B.4c})$$

where x , y , and z are cartesian coordinates, r is the distance from the origin, and the magnetic dipole is oriented up and positioned at the origin [NASb].

C Magnet Slot Radius

The magnets we purchased were advertised as having a quarter-inch diameter, but in reality they deviate a little bit. We needed to measure the magnets' actual diameter and height. On average, we measured the magnet's diameter to be 6.274 mm, and its height to be 6.31 mm. The radius, then, was 3.14 mm. However, the 3D printer does not print magnet slots of the exact radius specified in the CAD model. Therefore, we also needed to find out how does the radius specified in the model relate to the radius actually printed for the magnet slot. This appendix tells how we accomplished this.



Figure C.1: A 3D print was made with magnet slots of varying radii, starting from 3 mm, stopping at 3.5 mm, and going up by $(1/32)$ mm with each slot.

To find the optimal radius for the slot to fit the magnet just tightly enough, the test tray in Fig. C.1 was designed and printed. The radii in the test tray started from 3.0 mm and went up by $1/32$ mm with each slot until 3.5 mm. As it

Table C.1: The magnet slot test tray, where each slot was given one radius in the CAD model, but ended up with a slightly different radius due to 3D printing imperfections.

Increment	Model R (mm)	Printed R (mm)	Notes
0	3.00	2.85	
1	3.03	2.90	
2	3.06	2.91	
3	3.09	2.96	
4	3.13	2.97	
5	3.16	3.06	
6	3.19	3.02	
7	3.22	3.10	
8	3.25	3.09	
9	3.28	3.13	
10	3.31	3.21	Magnet fits very barely, and gets stuck.
11	3.34	3.25	Magnet fits snugly.
12	3.38	3.34	
13	3.41	3.30	Magnet fits loosely.
14	3.44	3.36	
15	3.47	3.39	
16	3.50	3.43	

turned out, at a slot radius of $(3 + 10/32)$ mm, the magnet barely fit, and it was very difficult to take it out. This made that radius perfect for the Setup-3 slots used in this thesis. The details of the magnet slot size test may be found in Table C.1.

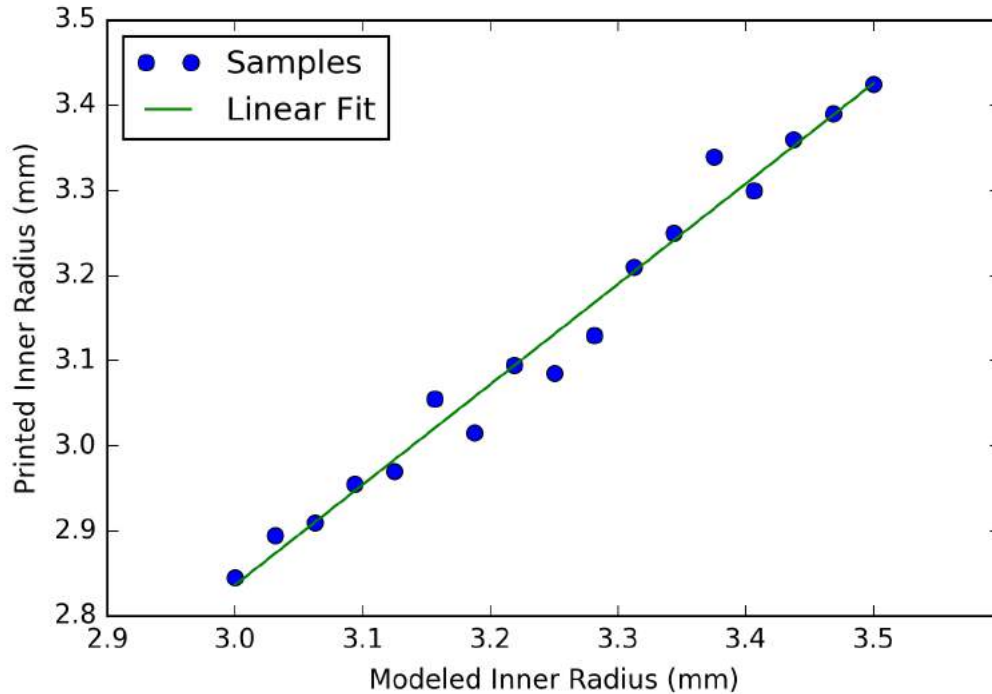


Figure C.2: Slots of different sizes for holding our quarter-inch magnets were measured, and a linear relation between the slot size as modeled in CAD and the slot size as printed was found.

We had the perfect slot size figured out, but we noticed that the relation between printed and model radius looked linear for the radius range 3.0 mm to 3.5 mm. Therefore, we fit a line, obtaining Fig. C.2. Numerically, the result was:

$$P = (-0.70 \pm 0.14 \text{ mm}) + (1.18 \pm 0.04) M, \quad (\text{C.1})$$

where P is the printed inner radius, and M is the modeled inner radius. This result is only usable for small slots roughly the size of a quarter-inch magnet; the equation yields absurd values for P when used on M values far outside this limit. Nevertheless, Fig. C.2 and Eq. C.1 give us a correction relation that we may use to find the radius we should use in our CAD model if we want a hole roughly the

size of a magnet to print accurately.

D Optimizing Magnet Arrangement

This chapter is meant to be a guide to using our project’s Python code to optimize a magnet arrangement. The code may be downloaded from:

<https://gitlab.com/ruvim.k.1/Stability-Keplerian-Flow-2017/raw/master/Permanent-Files/t17/User-Optimize-Code.zip>

Our code requires Python with scientific libraries (NumPy, etc.). An easy way to acquire all the libraries with Python is to download the Anaconda package. Installing Anaconda is not difficult, so we leave the procedures for that up to the reader to figure out. Our code also requires the Bokeh package, which does not come pre-installed with Anaconda. The first section will guide the reader through the brief process of installing Bokeh, while Section D.2 instructs the reader on how to use our code (no programming required!) to optimize a magnet arrangement.

D.1 Installing Bokeh

One of the prerequisites to run the Python user-optimize code is to have a package named “Bokeh” installed on the system. If it is not installed, Python will throw an import error. Fortunately, installing it is extremely easy.

The most straight-forward method to install Bokeh is using the Anaconda install command. Open a Terminal on Linux (using `Ctrl + Alt + T`), or the Command Prompt on Windows (Windows: first use `Win + R`, then type “cmd”, and then hit Enter).

Next, type the following command:

```
conda install bokeh
```

If Anaconda is installed, and if all works well, then Bokeh should now be installed, allowing our `user-optimize.py` to run.

D.2 Using Python Code

Once the ZIP archive is downloaded and extracted, it may be easily run. If on Linux, open a Terminal (Ctrl + Alt + T), change into the directory with the `user-optimize.py` Python script, and run the following:

```
bokeh serve --show user-optimize.py
```

If on Windows, we have provided a batch script with the above command saved in it. Simply double-click the “`user-optimize.bat`” file to launch the Python program.

We thought about what would be the best form of user input, and we searched online for libraries that allow for interactive plots in Python. *Bokeh* seemed attractive because it can be used to create sliders. All the user would have to do is slide a slider and watch the graph change. We installed Bokeh on the Borrero Lab computer and built the interface shown in Fig. D.1. The sliders on the left control the height of each magnet ring below the XY-plane, and the sliders on the right control the radius of each ring. The radius is in mm, but the height is in reciprocal length units to make fine-tuning the magnetic field easier. These units are converted back to mm before being saved to the CSV spreadsheet. There is currently no way to adjust the rotation angles from the user interface, so these must be adjusted manually in the spreadsheet that the Python code saves to. The “Water Z” slider controls how high the water level is above the XY-plane, the default being 0. This slider was created because we needed to see how a mistake in the water level height can affect the magnetic field profile at the water’s surface.

Fig. D.2 shows the feedback part of the `user-optimize` Python tool we developed to assist us in optimizing for the magnet arrangement in Setup-3. In the plot, the purple dots represent our physical measurements of what the magnetic field actually was. These were not there when we were designing the magnet arrangement; they appear only after we build the setup and take and record measurements of the magnetic field. When we built the setup, the physically-measured magnetic field was, for the most part, only about 80% of the predicted field, so

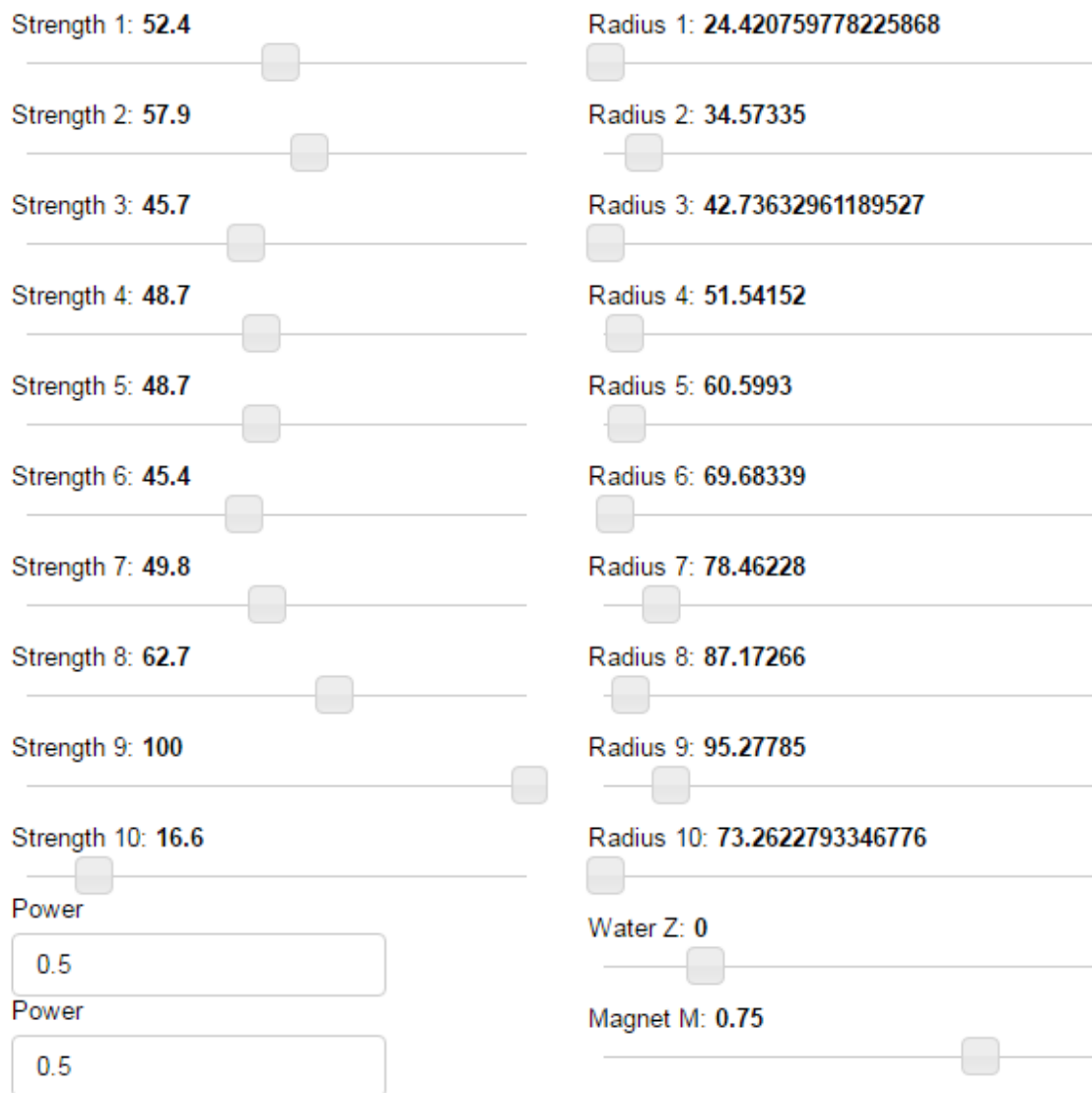


Figure D.1: The Bokeh library allowed us to create sliders and text input for allowing the user to optimize the magnet arrangement parameters.

we set the M to be 80% of the original M for that plot for Setup-3. The two sliders, “Water Z” and “Magnet M”, are there mainly for checking to make sure the water is positioned correctly vertically and the magnetization constant M is calculated correctly. The “Magnet M” slider controls how much to scale the magnets’ magnetization constant by before calculating the predicted magnetic field to put in the plot.

We know that our optimized magnetic field has the desired power profile because of the thick blue template lines. The templates are just square-root curves scaled up to fit the data, for the purple dots, and the predicted curve, for the green curve. There are both components in this plot, so there are two template curves in the background. These template curves are meant mainly for the optimization part of the workflow. When dragging the sliders to move magnet rings around, the user tries to make the green curve match the thick blue template behind it. The default template is $\propto r^{0.5}$ (square-root), but that can be changed by changing one or both of the text inputs that say “Power” and “0.5”, seen in Fig. D.1. The “0.5” means to shape the template as $r^{0.5}$; “1.5” would have made $r^{1.5}$, and so on. As seen here, the template curve is useful for finding the optimal magnet arrangement.

One other important part of the user-optimize tool is the physical magnet arrangement plotted at the bottom, also seen in Fig. D.2. The code plots magnets as light-pink rectangles, the water surface as a thin, horizontal, blue line, and the floor of the water cell as the horizontal black line underneath that. These are as important as the template curves because without them, the user cannot see if they are spacing magnets apart enough, or if the magnets are close to overlapping in space.

The first time the Python program is downloaded and run, it will show only the overall parameters’ sliders (power, water level, and magnetization). However, behind the scenes, user-optimize creates two folders: Optimized-Params and User-Optimize. Therefore, when running it for the first time, do the following:

1. Close the browser window or tab that has the Bokeh interface. Close the Terminal or Command Prompt window that was opened earlier for launching the Python script. This is to avoid data loss problems related to overwriting saved data.
2. Open the “Optimized-Params” folder.
3. Double-click on the “magnet-arrangement.csv” file - it should open with either Microsoft Office Excel or LibreOffice Calc.
4. If a dialog box comes up with import options, as in Fig. D.3, ensure the “Tab” and “Comma” checkboxes are checked, and click OK.
5. There should open a spreadsheet with no rows other than the header with column labels. Under the “Magnets in Ring” column, insert some magnet counts, however many magnets whichever ring should have. For example, if the first ring should have 12 magnets, type “12” and hit Enter. Repeat for however many rings need to be added. If a ring needs to be south-side up, then enter a “-1” in the ring’s row under the “Orientation” column.

6. Filling out the other columns (ring radius, height, etc.) is okay, but it is not required - the `user-optimize` script will fill in missing values with defaults.
7. Save the spreadsheet back to the same CSV file, and *close the spreadsheet window* to avoid data overwrite problems.
8. Open the Python program again.
9. Voila! There should now be controls for changing the added rings' "strength" (a one-over-radius scaled value) and radius.

For an existing magnet arrangement CSV file, just open it with Excel or Calc to manually view or edit the parameters, or run the Bokeh Python script to see what the predicted magnetic field looks like. After building the magnet arrangement as a physical setup and measuring the magnetic field with a gaussmeter, the measured values may be saved as a text file into the same folder as "`user-optimize.py`" in order for `user-optimize` to recognize the measurements and plot them on top of the predicted curve, as in Fig. D.2. The text file should be named "`measurements.txt`," and it should have one measurement recorded per line, while each line is of the format: relative radial position (mm), tab-space, magnetic field (gauss). So, in other words, it is a tab-delimited CSV file with the radial position and magnetic field as the columns.

The code treats the radial positions in "`measurements.txt`" as relative positions, and it adds 18mm to them to obtain absolute positions. This is for easier data entry when measuring the magnetic field. The position is easier to measure from the center cylindrical part than from the center. To change this 18mm to some other offset, save a number (for example, "18") as a new file called "`meas-offs.txt`". The `user-optimize.py` will check for a file with that name, and it will use the number it reads as an offset for the radial positions. The units are mm, but do not include them in the "`meas-offs.txt`" file.

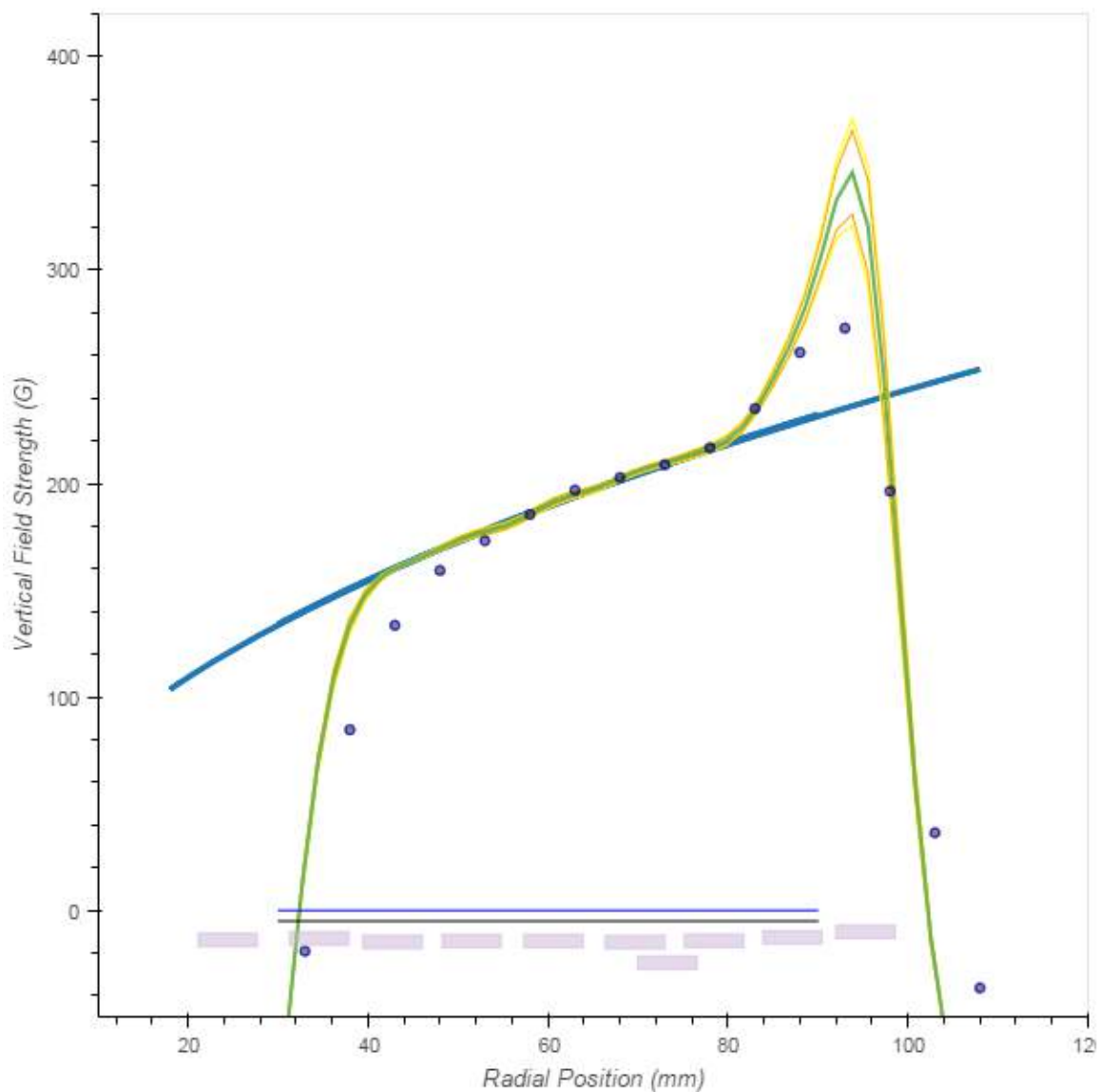


Figure D.2: The Bokeh plot of the theoretical predicted magnetic field. The code takes a few regularly-spaced azimuthal angles and computes radial field profiles for each. In the plot, green is the mean of these profiles. Orange is the mean profile plus and minus the standard deviation of the profiles. Yellow is the maximum and minimum fields, taken from these sample profiles. The purple dots are the measured magnetic field samples from “measurements.txt,” and the thick blue are the template curves. Horizontal units are mm. This is the interactive plot that the user actually sees when changing the sliders shown in Fig. D.1. The pink rectangles are magnets below the XY-plane, the horizontal blue is the water surface, and the horizontal black is the water cell’s floor, assuming a water depth of 5 mm; the vertical units for all these objects are mm. So, this plot is the feedback part of the tool that we used to optimize for Setup-3.

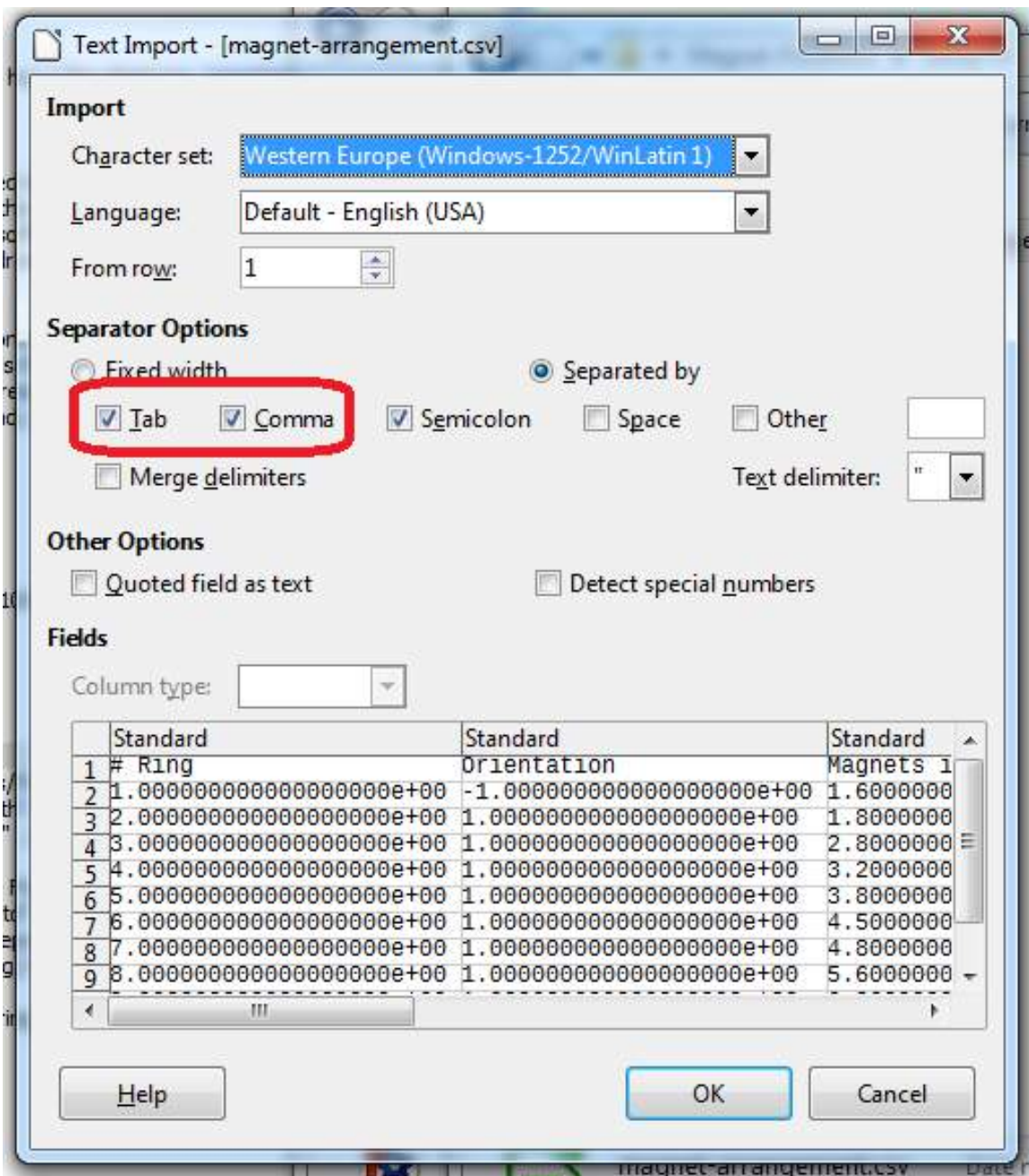


Figure D.3: The “magnet-arrangement.csv” file shows the arrangement parameters that can be copy-pasted to FreeCAD.

E Parameters for Setup-1, Setup-2, and Setup-3

This chapter provides the parameters used for Setup-1, Setup-2, and Setup-3. The Setup-2 was never built, but its parameters are still shown just so the reader can see why it was not built.

The code optimized the magnet ring radius, R_i , height, H_i , and rotation angle, A_i , for each ring with number i , and gave us a state vector with the optimal parameters. The number of magnets in the i th ring is denoted as N_i in our parameter table. Our code was not smart enough to take magnet orientations into account back when we were designing Setup-1, so all the magnets were pointed north (N) up. All the parameters for Setup-1 are shown in Table E.1.

We optimized Setup-2 and Setup-3 ourselves, using the sliders in our Python tool. Setup-2 parameters are shown in Table E.2. After designing Setup-2 with maximum field profile smoothness in mind, we realized it is too complicated. It has 15 rings, and the rings are arranged in such a way that 7 of them are beneath the other 8, making multiple layers of rings. Because of the complexity, we created another magnet arrangement, Setup-3, with fewer magnet rings and a simpler ring arrangement. We decided to set the orientation of ring 1 to be south (S) up because we hoped that will help smooth the curve a little more. Our code became more advanced by the time we designed Setup-3, so we were able to adjust the rings' orientations by then as well. Optimizing for Setup-3, we noticed that picking the highest N_i possible for the desired ring radius (larger rings can fit larger N_i) is key to making the curve as smooth as possible, so we kept increasing N_i as much as we could with each additional ring. After we were done optimizing the curve for the most part, we finally made a finishing touch of picking a value to set A_2 to, such that the curve was a little bit smoother; we left the A_i at 0 for the others because changing them would not have contributed much to making the field smoother. All the parameters for Setup-3 are shown in Table E.3.

Table E.1: Magnet arrangement parameters' optimization results for Setup-1. The variables are i , the ring number, N_i , the number of magnets in the i th ring, R_i , the radius of the ring, H_i , the height of that ring, and A_i , the angle by which the ring should be rotated about the Z-axis.

i	Up Side	N_i	R_i (mm)	H_i (mm)	A_i (rad)
1	N	8	16.92	24.64	2.95
2	N	16	61.87	49.96	0.20
3	N	16	41.88	52.31	0.00
4	N	16	32.84	40.75	0.00
5	N	16	72.97	52.15	0.01
6	N	32	102.11	48.82	0.00

Table E.2: Magnet arrangement parameters for Setup-2. The variables are i , the ring number, N_i , the number of magnets in the i th ring, R_i , the radius of the ring, H_i , the height of that ring, and A_i , the angle by which the ring should be rotated about the Z-axis.

i	Up Side	N_i	R_i (mm)	H_i (mm)	A_i (rad)
1	N	8	25.11	12.93	0
2	N	16	37.62	24.54	0
3	N	24	44.63	14.66	0
4	N	32	54.54	15.23	0
5	N	20	34.63	14.73	0
6	N	32	59.74	25.16	0
7	N	32	63.94	15.09	0
8	N	32	73.24	14.33	0
9	N	48	92.66	11.36	0
10	N	48	75.56	23.77	0
11	N	48	83.16	13.45	0
12	N	48	73.26	34.50	0
13	N	16	41.72	36.04	0
14	N	16	45.72	45.13	0
15	N	48	82.76	37.01	0

Table E.3: Magnet arrangement parameters for Setup-3. The variables are i , the ring number, N_i , the number of magnets in the i th ring, R_i , the radius of the ring, H_i , the height of that ring, and A_i , the angle by which the ring should be rotated about the Z-axis.

i	Up Side	N_i	R_i (mm)	H_i (mm)	A_i (rad)
1	S	16	24.42	13.81	0
2	N	18	34.57	13.14	0.087
3	N	28	42.74	14.79	0
4	N	32	51.54	14.33	0
5	N	38	61.00	14.33	0
6	N	45	69.68	14.84	0
7	N	48	78.46	14.17	0
8	N	56	87.17	12.63	0
9	N	60	95.28	10.00	0
10	N	48	73.26	24.54	0

F Our 3D Parts in FreeCAD

This appendix chapter is meant to be a guide on how to use FreeCAD to make 3D CAD models similar to the ones that were used in this thesis. We explain why we chose FreeCAD, describe the user interface, and provide the step-by-step instructions on making a magnet tray similar to Setup-3. The parts are available for download at:

<https://gitlab.com/ruvim.k.1/Stability-Keplerian-Flow-2017/raw/master/Permanent-Files/t17/FreeCAD-Files.zip>

A little bit about why we chose FreeCAD. We had to choose a 3D CAD software for designing our models. We considered AutoDesk Fusion 360, OnShape, Blender, and FreeCAD. Fusion 360 and OnShape require sign-up and are web-based. Web-based software has the limit of how fast the browser can run it, but we wanted software that would run natively on the operating system and not be slowed by browser and JavaScript limits. Blender is such a software that runs natively, but it offers essentially no ability to change objects' dimensions once they are created. We still used Blender for assembling artistic drawings, such as the ones in Fig. 3.1, but, for technical drawings, FreeCAD was left.

FreeCAD has a nice user interface, shown in Fig. F.1. The user interface has so many controls that they would not all fit on one toolbar. Thus, FreeCAD categorizes the controls into what are called *workbenches*, and shows the user only the controls that belong to the selected workbench. The workbench selection is near the top-right; it is that drop-down menu that says “Part” in the screenshot. The most interesting workbenches to us are the “Spreadsheet,” “Part Design,” and “Part.” For navigation, click-drag the middle mouse button (MMB) to move around, and shift-right-click and drag the right mouse button (RMB) to orbit. Scroll (MMB) to zoom on the part. To select a face (one flat side) of an object, click on the face in the 3D viewport. Click again to select the whole object. Alternatively, click on an object's name in the tree view (a hierarchical view of the

CAD file on the left) to select the whole object.

Once the magnet arrangement parameters are figured out using user-optimize, follow the steps to make the CAD model:

1. Open the “magnet-arrangement.csv” file generated by the user-optimize Python code. Double-clicking the CSV file will probably bring up a dialog similar to the one shown in Fig. D.3; ensure the “Tab” and “Comma” checkboxes are checked, and click OK. A new spreadsheet window should open with all the parameters.
2. Download and extract the ZIP archive with the starting-point FreeCAD files at: <https://gitlab.com/ruvim.k.1/Stability-Keplerian-Flow-2017/raw/master/Permanent-Files/t17/FreeCAD-Files.zip>
3. Open “magnet-tray-starting-material.FCStd”; if it does not open with FreeCAD but rather an “Open with” dialog pops up, choose “Select a program from a list of installed programs,” browse to the FreeCAD folder, then to the “bin” folder, and choose “FreeCAD.exe” , whose icon is a red “F” with a blue gear next to it.
4. Save this as a new FreeCAD file. Go to the “File” menu, then “Save As,” and save it somewhere, in case FreeCAD crashes.
5. In the workbench selection drop-down, switch into the “Part” workbench. This is required to use the “Boolean” tool.
6. Double-click on the “Params” spreadsheet in the tree view.
7. Choose a total height for the magnet tray (must fit all magnets vertically), and enter it into the “Total Tray Height” row’s “Value” column.
8. Go back to the file browser window with the FreeCAD files, and double-click on the “one-ring-hole-v1.FCStd” file; it should open in FreeCAD in a new window. The ring might be out of view when first opened, but use the MMB to zoom out to see the whole ring.
9. Open the spreadsheet; this may be done by double-clicking the “Params” spreadsheet item under “one-ring-hole-v1” in the tree view near the top-left, as seen in Fig. F.2.
10. Enter the same total tray height from step 7 into this spreadsheet.
11. Also in this spreadsheet, under “Water Cell Floor Thickness,” make sure the floor thickness is correct. Also check the “Water Level” value.

12. For each ring of magnets (each row of the parameters table), perform steps 13 through 30:
13. Go to the window opened in step 8.
14. Go to the spreadsheet from step 1. Copy the number from the “Magnets in Ring” column.
15. Go to the ring-hole window from step 8. In the spreadsheet, click the cell in the “Value” column and the “Number of Magnets in the Ring” row. At the top of the spreadsheet, there is a text input called “Contents;” click inside it, hit Ctrl-A to select all, hit Backspace, and then hit Ctrl-V to paste the value from the spreadsheet. If the value pasted has a space after it, hit Backspace to remove it (for some reason FreeCAD complains when there is an invisible newline character pasted with the value, but this seems to fix it; spaces are fine, but pasting from a spreadsheet seems to insert invisible newline spaces that give FreeCAD trouble). Hit Enter to set the cell’s value.
16. Again, go to the spreadsheet from step 1. Copy the number from the “Radius (mm)” column.
17. Return to the window from step 8, and follow *most* of step 15 but for the “Ring Radius” row of the FreeCAD spreadsheet. The difference here is that this radius value should have units. Thus, after hitting Backspace to remove extra space, but before hitting the final Enter, type “mm” into the text input. So, in other words, paste the number representing the radius, hit Backspace to remove extra space, type “mm”, and hit Enter. The “mm” lets FreeCAD know that it should treat the value as a length in millimeters.
18. Follow the same steps 16 and 17 to copy the ring height (units are mm) into FreeCAD.
19. Follow steps 14 and 15 to copy the ring rotation angle (as far as FreeCAD is concerned, this one is dimensionless!) about the Z-axis into FreeCAD.
20. Finally, here is the step where thinking is involved: choose whether or not a spacer is needed for this ring, and enter a “1” (yes) or “0” (no) into the “Use Spacer” row in the FreeCAD spreadsheet. This just affects how the resulting ring area is shaped. We used “1” for all rings except the deep ring number 10 in Setup-3, which would mess up the magnet tray if we would have used a “1” for that ring.
21. See the tabs at the very bottom of the window. Click on the “one-ring-hole-v1” tab with the FreeCAD icon to see how the model looks.

22. In the tree view near the top-left, click on “AntiRing” to select it.
23. Hit **Ctrl + C** to copy the selection. When prompted to copy the dependencies, click “Yes” to copy them too (since we are about to paste the selection into a different FreeCAD model).
24. Go to the FreeCAD window from step 3.
25. Hit **Ctrl + V** to paste.
26. In the tree view, click on “StartingPart” to select it. Then **Ctrl**-click the “AntiRing” part that was just pasted.
27. On one of the toolbars at the top, there should be an icon with two blue balls next to each other; hovering the mouse over that icon shows a tooltip, saying “Run a boolean operation with two shapes selected.” This is the boolean tool. Click on it.
28. Select the “Difference” radio button, and click “Apply.” Then click “Close” next to “Apply.”
29. Congratulations! You have cut out the slots and the rescue holes for a ring of magnets! Hit **ctrl-S** to save your work in case FreeCAD crashes!
30. In cutting out more rings, select the latest part (rather than the original “StartingPart”) in step 26.
31. After all the rings are subtracted in this way, select the resulting finished part. Go to the “File” menu, and select “Export;” or hit **Ctrl + E**. Choose “STL” for the export format.
32. The STL file may be 3D printed from the Cura software, but be sure to first flip the piece over in Cura - the exported STL will be upside down!
33. To flip the part in Cura, click on it. Click “Rotate” at the bottom, and drag one of the axes until Cura says “180” next to the cursor. If no rotation seems to be happening, you may have selected the vertical axis to rotate about; try a different axis.
34. Note that, depending on the number of magnet slots and overall complexity, it may take Cura up to 5 or 10 minutes to generate the 3D printer GCode. Please be patient.
35. You’re done!

That was the magnet tray. For the water cell, open the “water-cell-v6.FCStd” file and double-click on the “CellParams” spreadsheet in the tree view. Change any parameters necessary, such as the water inner or outer radius, or the floor thickness. Be sure that the floor thickness and water level from here is equal to the same values entered in step 11 above. To export it for 3D printing, go to the tree view and select the three parts: “CenteringShell,” “AirflowShield,” and “PartTop-WaterCellWithBothWallWindows.” Then use the “File” menu or hit **Ctrl + E** to export an STL.

To learn how to design parts from scratch, see the FreeCAD tutorials, such as the Part Design tutorial [Fre]. The tutorial by Mark J. Norton is a little bit old now, but it is also quite useful [Nor11].

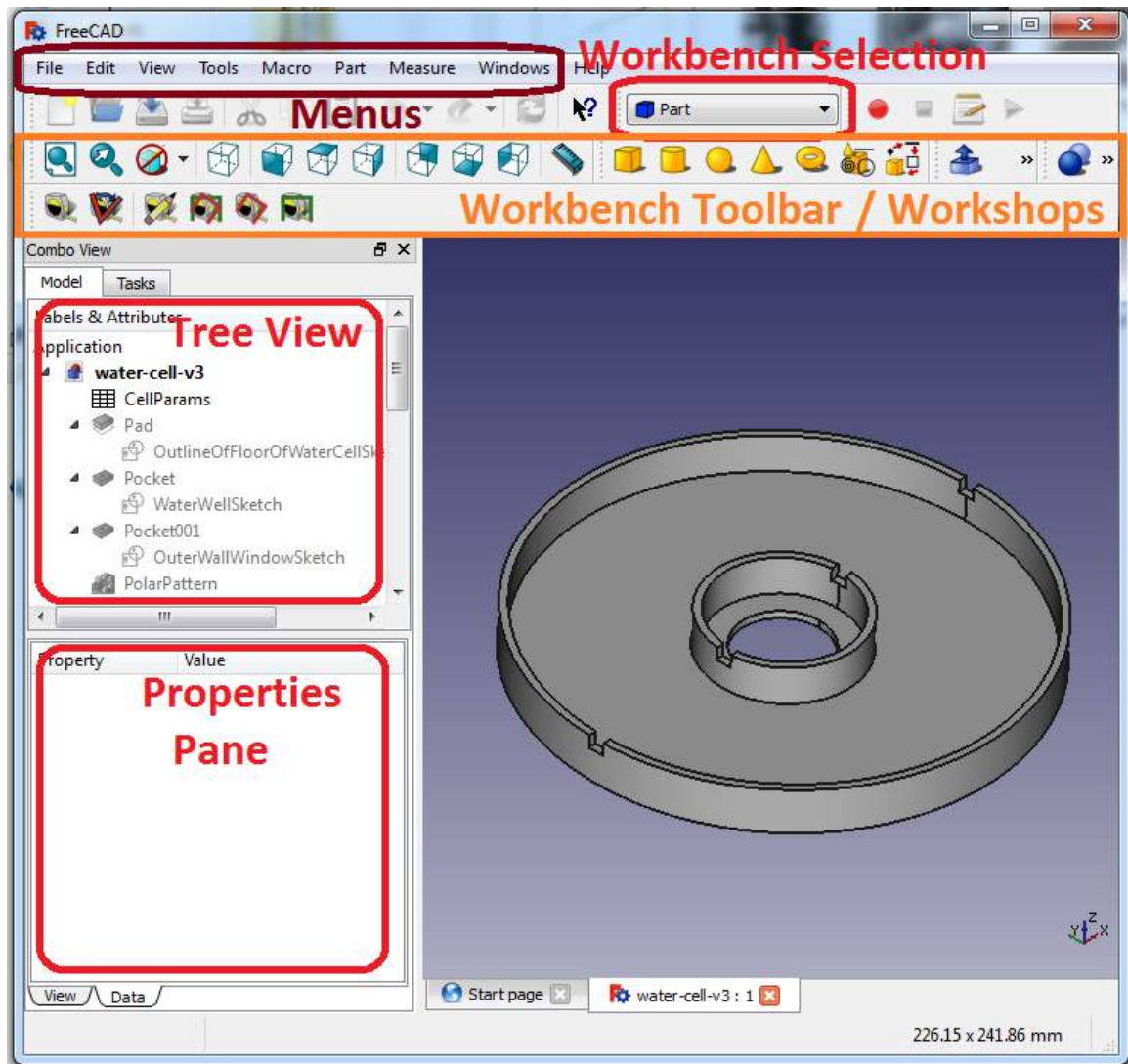


Figure F.1: The FreeCAD user interface. FreeCAD is still in early stages of development, but it is quite useable and has a few features.

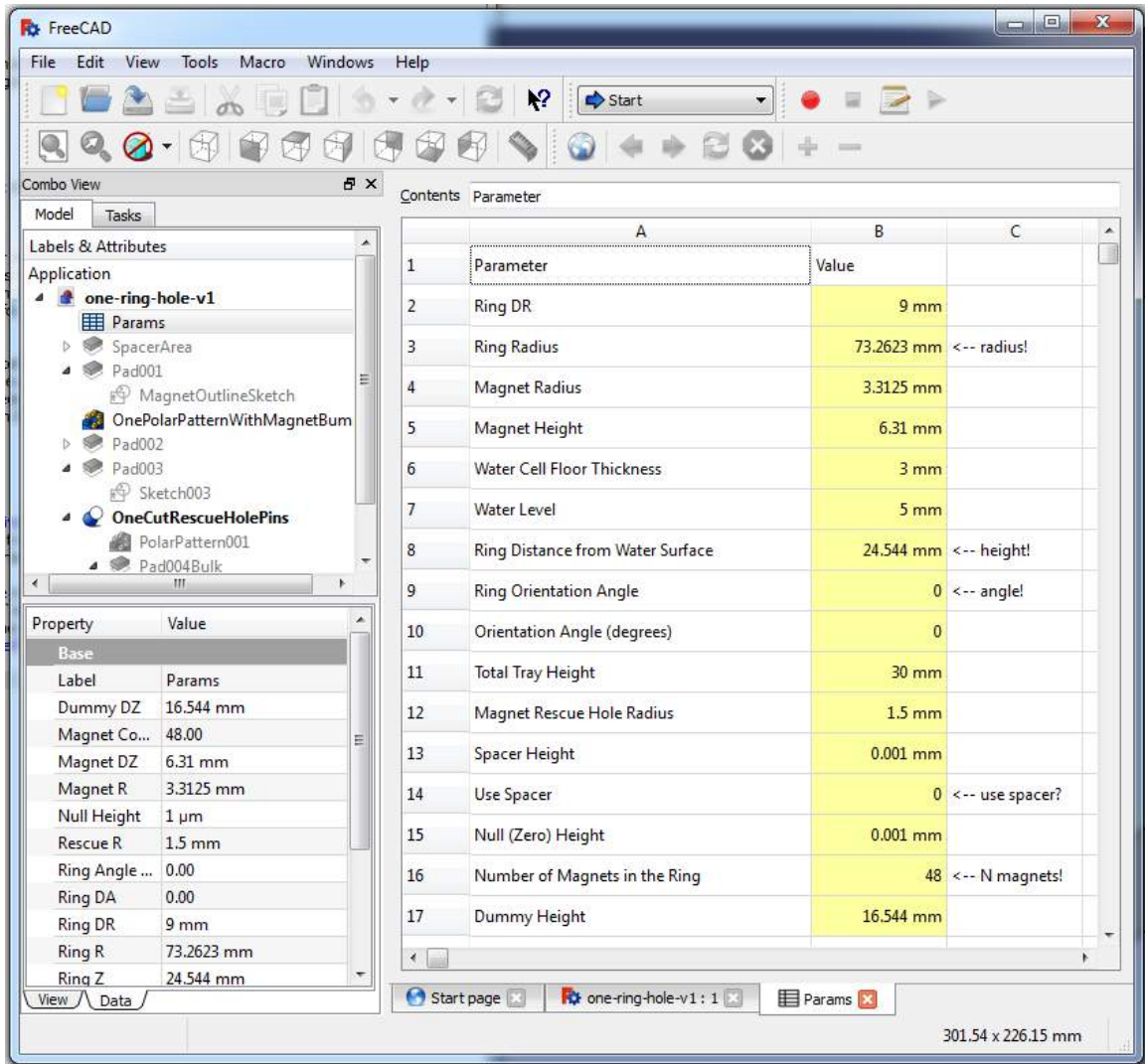


Figure F.2: The “one-ring-hole-v1” FreeCAD file has a spreadsheet with editable ring parameters.

G Taking Data

We recorded video frames using the uEye camera connected to the computer. The software to capture images from the camera came with the uEye software package, but it lacked a “Save” button, which we added. Our executable may be downloaded in a ZIP archive from:

```
https://gitlab.com/ruvim.k.1/Stability-Keplerian-Flow-2017/raw/master/Permanent-Files/t17/uEye-Sequencer-x64bin.zip
```

The source code may be downloaded from:

```
https://gitlab.com/ruvim.k.1/Stability-Keplerian-Flow-2017/raw/master/Permanent-Files/t17/uEye-Sequencer-Source.zip
```

The instructions how to use this may be found at the end of this chapter.

The IDS uEye software package had sample programs, and luckily, the source code was there too. The uEye Sequencer sample program was suitable because it captures image sequences into memory, without compression, in their original quality. It did not come with a “save images” button, so we went into the source code and added a “save” button. After compiling it with Visual Studio, we were able to capture 1250 frames (25 seconds) at a time, and then save them as bitmap (BMP) sequences in their own folders. The user interface, with the button we added, are shown in Fig. G.1.

The maximum of frames that could fit in memory on the computer was around 1400 or so, but 1400 is 28 seconds, which is not as much of a round number as 25 seconds. The camera’s default framerate is 50 frames per second, and the number of frames to capture was the only user-editable option that came with uEye Sequencer. The rest of the settings were loaded from the camera driver’s

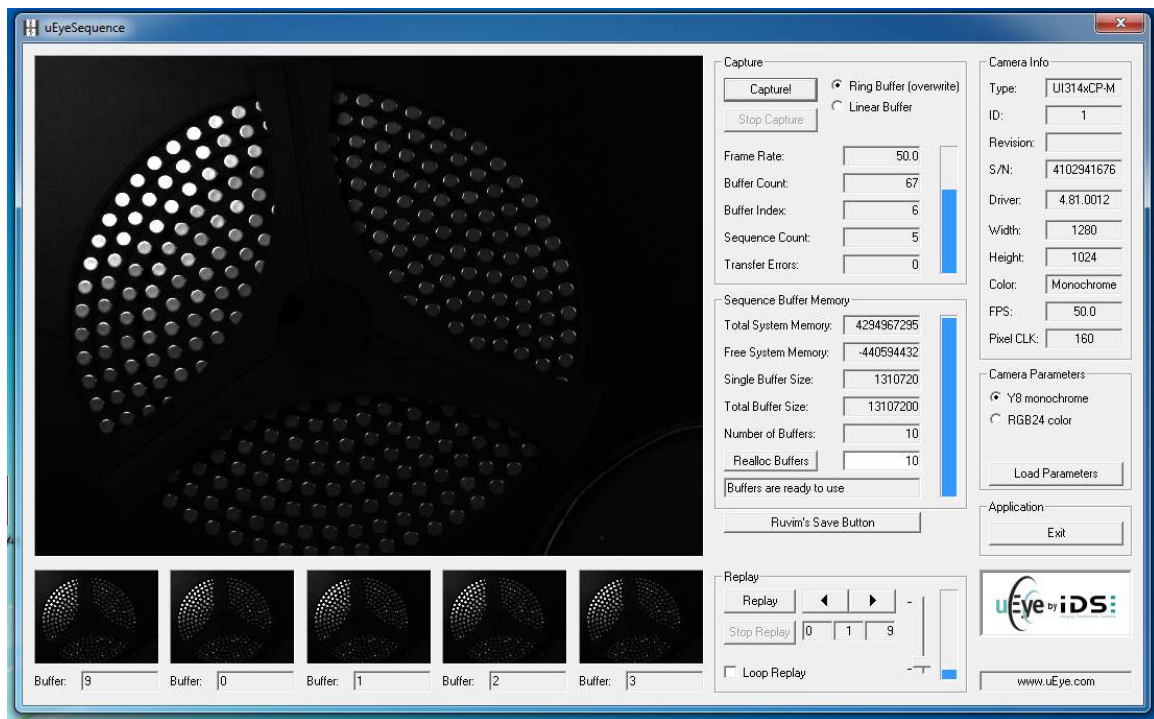
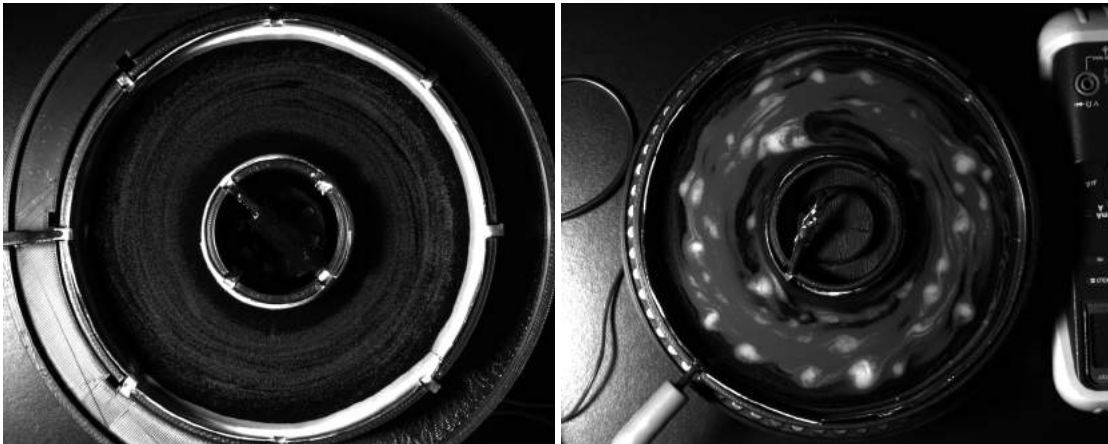


Figure G.1: We added a “Save” button to the uEye Sequencer sample program’s source code, and we used that to capture images from the camera.

defaults. Even though we were unable to change any other parameters, we were okay because it made sense to just use those parameters loaded from the camera; those parameters are what the camera was designed to perform best with. The image resolution was 1280 by 1024 pixels. We used the “Y8 monochrome” color parameter, which meant the bit depth was 8 bits. We captured 1250 frames at a time. The LED light grid was turned up to be bright, but not as bright as to saturate the pixels. Fig. G.2 shows the first frame captured from each setup’s recorded image sequence.

To use the uEye Sequencer, perform the following after opening it:

1. There is a “Realloc Buffers” button near the bottom third of the controls. In the number input box next to it, change the number to the desired number of frames (for example, 1250). Push the “Realloc Buffers” button.
2. To continuously “preview” what’s on camera, ensure the “Ring Buffer” radio button at the very top is checked, and click “Capture.”
3. To record a set of frames, ensure “Linear Buffer” is selected and click “Capture.”



(a) Setup-1

(b) Setup-3

Figure G.2: The first frame captured for each setup.

4. After recording stops, click the “Save” button. In the dialog that opens, browse to a new folder where the image sequence should be saved. Type the filename for frame 1 (for example, type “frame0001”), and click “Save.”

H Linear Regression

The equations in this appendix may be found in Taylor's Error Analysis, but they are provided here for the reader's convenience [Tay97]. For the fits, the least-squares fit was done to calculate the F_A and F_B fit parameters for the line equation $y = F_A + F_Bx$, using

$$F_A = \frac{1}{\Delta} \left(\sum x^2 \sum y - \sum x \sum xy \right) \quad (\text{H.1a})$$

$$F_B = \frac{1}{\Delta} \left(N \sum xy - \sum x \sum y \right) \quad (\text{H.1b})$$

$$\Delta = N \sum x^2 - \left(\sum x \right)^2 \quad (\text{H.1c})$$

where x and y are the data samples, and N is the number of data samples [Tay97]. The Δ is a common factor for calculating both fit parameters, so it is factored out as its own term for convenience.

To find the uncertainties, σ_A and σ_B , in the fit parameters F_A and F_B , we used

$$\sigma_A = \sigma_y \sqrt{\frac{\sum x^2}{\Delta}} \quad (\text{H.2a})$$

$$\sigma_B = \sigma_y \sqrt{\frac{N}{\Delta}} \quad (\text{H.2b})$$

$$\sigma_y = \sqrt{\frac{1}{N-2} \sum_{i=1}^N (y_i - F_A - F_B x_i)^2} \quad (\text{H.2c})$$

where σ_y is the uncertainty in the measurements of y given the fit parameters F_A and F_B [Tay97]. Fitting a line to data samples that have large uncertainty in both x and y is controversial, but these equations work as long as the error in x

is much smaller than the error in y .

We also needed to find weighted averages in this thesis. From Taylor Chapter 7, section 2, “Weighted Averages,” a weighted average is taken by [Tay97]:

$$x_{wav} = \frac{\sum w_i x_i}{\sum w_i} \quad (\text{H.3})$$

where w_i is the weight of the i -th value, x_i , in the data set. The weight is defined as

$$w_i = \frac{1}{\sigma_i^2} \quad (\text{H.4})$$

where σ_i is the uncertainty of x_i . Finally, the uncertainty of the weighted average itself is

$$\sigma_{wav} = \frac{1}{\sqrt{\sum w_i}}. \quad (\text{H.5})$$